Mechanisms of MTOC clustering and spindle positioning in the budding yeast *Cryptococcus neoformans*: a microtubule grow-and-catch model

Saptarshi Chatterjee[1], Subhendu Som[1], Neha Varshney[2¤], Kaustuv Sanyal[2*], Raja Paul[1**]

1 School of Mathematical and Computational Sciences, Indian Association for the Cultivation of Science, Kolkata -700032, India
2 Molecular Mycology Laboratory, Molecular Biology and Genetics Unit, Jawaharlal Nehru Centre for Advanced Scientific Research, Jakkur, Bangalore -560064, India
¤Current Address: Ludwig Institute for Cancer Research, Department of Cellular and Molecular Medicine, University of California San Diego, La Jolla, CA 92093, USA

* sanyal@jncasr.ac.in ** raja.paul@iacs.res.in

Abstract

Mitotic spindle formation in the pathogenic budding yeast, *Cryptococcus neoformans*, depends on multitudes of inter-dependent interactions involving kinetochores (KTs), microtubules (MTs), spindle pole bodies (SPBs), and molecular motors. Before the formation of the mitotic spindle, multiple visible microtubule organizing centers (MTOCs), coalesce into a single focus to serve as an SPB. We propose a 'grow-and-catch' model, in which cytoplasmic MTs (cMTs) nucleated by MTOCs grow and catch each other to promote MTOC clustering. Our quantitative modeling identifies multiple redundant mechanisms mediated by a combination of cMT-cell cortex interactions and inter-cMT coupling to facilitate MTOC clustering within the physiological time limit as determined by time-lapse live-cell microscopy. Besides, we screened various possible mechanisms by computational modeling and propose optimal conditions that favor proper spindle positioning - a critical determinant for timely chromosome segregation. These analyses also reveal that a combined effect of MT buckling, dynein pull, and cortical push maintain spatiotemporal spindle localization.

Author summary

Cells actively self-assemble a bipolar spindle to facilitate chromosomal segregation. Multiple MTOCs, on the outer nuclear envelope, cluster into a single SPB before spindle formation during semi-open mitosis of the budding yeast *Cryptococcus neoformans*. Eventually, the SPB duplicates and organizes the spindle to position it within the daughter bud near the septin ring during anaphase. In this work, we tested various computational models to match physiological phenomena in an attempt to find plausible mechanisms of MTOC clustering and spindle positioning in *C. neoformans*. Notably, we propose an MT 'grow-and-catch' model that relies on possible redundant mechanisms for timely MTOC clustering mediated by (a) minus end-directed motors that crosslink and slide anti-parallel cMTs from different MTOCs on the nuclear envelope and (b) a Bim1 mediated biased sliding of cMTs along the cell cortex toward the septin ring that pulls MTOCs in the presence of suppressed dynein activity. By combining an analytical model and stochastic MT dynamics simulations, we screened various MT-based forces to detect steady spindle positioning. By screening the outputs of various models, it is revealed that proper spindle positioning near the septin ring requires MT buckling from the cell cortex.

Introduction

Spatio-temporal dynamics of organelle-constituents relies primarily on the active organization of microtubules (MTs). MTs are semiflexible polymeric filaments having rapidly polymerizing plus ends and slowly polymerizing minus ends.

The growth and shrinkage of MTs are governed by intrinsic dynamic instability parameters [1]. In animal cells, the centrosome is a major MT nucleating center which forms a radial MT array [2–4] along with other membrane organelles such as the Golgi apparatus facilitating many noncentrosomal, radial MT networks [2, 5–9]. The cellular structures that harbor the ability to nucleate MTs and organize a radial network are often referred to as Microtubule Organizing Centers (MTOCs) [2, 10].

In the ascomycete budding yeast *Saccharomyces cerevisiae*, spindle pole bodies (SPBs), embedded on the nuclear envelope (NE) are analogous to centrosomes. The SPBs are enriched with distinct $\gamma-$tubulin receptors that organize the cytoplasmic MTs (cMTs) and nuclear MTs (nMTs) [11, 12]. The MT nucleation system in *S. cerevisiae* involves γ-tubulin small complexes (γ-TuSCs) and their receptors Spc110 and Spc72 [2, 12]. This MT nucleation system provides SPBs distinct nuclear and cytoplasmic domains indicating that a single MTOC can accommodate nucleation sites for both cMTs and nMTs [2, 10, 13].

Two major fungal phyla, Ascomycota and Basidiomycota [14–16] shared a common ancestor more than 500 million years ago [17]. While extensive studies have been carried out in the context of cell division in hemiascomycetous budding yeasts such as *S. cerevisiae*, the process of chromosomal partitioning in organisms belonging to Basidiomycota remains under-studied [14–16, 18]. A relatively better model basidiomycetous budding yeast is *Cryptococcus neoformans*, a human pathogen. This pathogen is responsible for life-threatening diseases including fungal meningitis and emerges as the 5th leading cause of mortality among the immuno-compromised individuals [19].

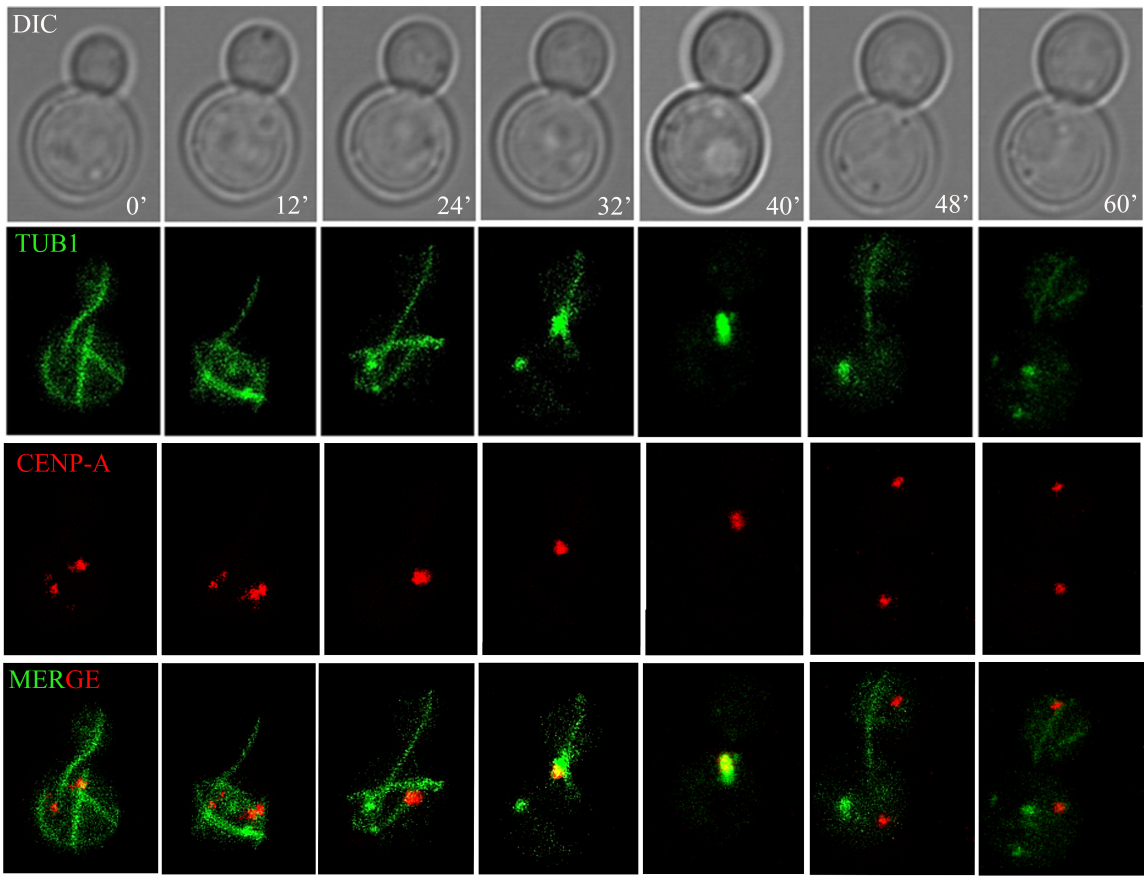

Fig 1. Cell cycle stages in *C. neoformans* wild-type cell as observed from live-cell imaging. Time series snapshots showing the localization of MTs (GFP-Tub1) and KTs (mCherry-CENP-A) at different stages of the cell cycle in a wild-type cell. The cell was subjected to time-lapse video microscopy for 60 min. The timestamp (in min) for each image is annotated in the DIC panel. Bar, 5 μm.

Like *S. cerevisiae*, cells divide by budding in *C. neoformans* as well (Fig 1, S1 Video). The major sequence of mitotic events from the formation of bud until chromosome segregation in *C. neoformans* can be categorized in the following temporal order: (a) Bud inception at the end of G1/onset of S phase [16], (b) clustering of KTs as a

single punctum at the periphery of nucleus after bud initiation [16] (Fig 1, S1 Video), (c) nuclear migration into the daughter bud followed by spindle formation; (d) localization of the spindle near the bud-neck junction/septin ring (Fig 1) and eventually (e) equal nuclear division mother and daughter bud (Fig 1, S1 Video).

While the overall process of nuclear division is conserved across Ascomycota and Basidiomycota, from a coarse-grained viewpoint, several intriguing differences exist in the spatio-temporal dynamics of MTOCs, KTs, nuclear migration, the specific location for spindle formation and nuclear division [14, 16, 20, 21]. We note these distinct differences in the following: (a) A single MTOC is found embedded on the NE at the onset of the cell cycle in ascomycetous budding yeast *S. cerevisiae* [22]. Here the MTOC serves as the SPB. At the G1/S phase, SPB duplicates and the KT-MT connections begin to form. However, the NE never breaks down, leading to closed mitosis [23, 24]. In contrast to *S. cerevisiae*, where the SPB being the only MTOC, several MTOCs are present in the basidiomycete budding yeast *C. neoformans* during interphase [14, 25, 26] (Fig 2A). Moreover, it undergoes semi-open mitosis marked by the transient breakdown/rupture of NE during metaphase to anaphase transition [15, 27]. (b) In *S. cerevisiae*, the KTs are grouped into a single cluster and KT attachments to the SPBs by MTs are maintained through most of the cell cycle [23, 28–30]. Contrary to that, in *C. neoformans*, KTs are unclustered during interphase [15, 16, 25]. As the cell advances through the cell cycle, the KTs gradually cluster into a single punctum, plausibly via various MT mediated interactions. Interestingly, a previous study [25] as well as our experiments (Fig 2A-2C) identify that the KTs colocalize with the MTOCs. The clustering of KTs into a single punctum and the clustering of MTOCs into a single SPB happen concomitantly (Fig 2A-2C). (c) In *S. cerevisiae*, prior to the chromosome segregation, the nucleus migrates to the proximity of mother-daughter bud neck junction [14, 16, 31, 32]. In *C. neoformans*, the sequence of events characterizing nuclear migration before the division is somewhat different from those of *S. cerevisiae*. First, the nucleus entirely moves to the daughter bud (S1 Fig). Second, the SPB duplication takes place either in the daughter bud or when the nucleus is migrated close to the bud-neck junction (namely the septin ring) as depicted in Fig 2A, Fig 2C. Subsequently, SPB biorientation, spindle formation, and localization of the spindle structure *inside the daughter bud near the septin ring* pave the way for proper division [14–16]. Interestingly, the features of having multiple MTOCs and nuclear division in the daughter bud are also characteristics of another basidiomycete yeast, *Ustilago maydis* [33]. Unlike budding yeast, the fission yeast *Schizosaccharomyces pombe* has a cylindrical rod-shaped geometry. Interestingly, *S. pombe* also possesses multiple interphase MTOCs (iMTOCs) and SPBs which nucleate MTs. During mitosis, fission yeast forms 3-5 MT bundles along the long axis of the cell organized by astral microtubules nucleated from duplicated SPBs and interphase MTOCs (iMTOCs). The purpose of the antiparallel MT bundles with minus ends overlapping at the middle of the cell and plus ends extending toward the cell tips is to position the nucleus at the cell center [34, 35]. In contrast, in *C. neoformans* the MTOCs fuse together to form the mature SPB while remaining attached to the NE. Nevertheless, the presence of multiple MTOCs in a basidiomycete budding yeasts *C. neoformans* and *U. maydis* could be reminiscent of fission yeast. Thus, *C. neoformans* may combine features of both budding and fission yeasts. However, while framing a mechanistic model of mitotic division in budding yeast *C. neoformans*, we took cue from our previous studies [14, 16] and extended the ideas of various force interactions from another budding yeast *S. cerevisiae* for its geometric similarity and similarities in cell cycle stages that lead to chromosome segregation.

Self-assembly of MTOCs is orchestrated by MT mediated 'grow-and-catch' (also known as 'search and capture') mechanism [14, 16]. Basic characteristics of the clustering mechanisms are shared across a diverse set of organisms as well as several organelle assemblies (e.g. Golgi assembly and stacking, mitochondrial assembly, multi-centrosomal clustering [36] etc.) and are not necessarily organism-specific [8]. The mechanics of MTOC clustering before the formation of the SPB in *C. neoformans* remains elusive and deciphering the same experimentally is challenging. The complete clustering in wild-type cells occurs within ~ 25 min since bud initiation (Fig. 2D-2E). In this context, we attempted to simulate possible mechanisms of MTOC clustering within the physiological time limit as determined experimentally by time-lapse microscopy.

In budding yeast *S. cerevisiae*, location for the mitotic division is predetermined even before the formation of the spindle [14, 21]. The spindle positioning within a confined geometry can often be mapped onto a centering problem across biological systems. For example, force transduction via the active force generators at the cell cortex leads to proper alignment and positioning of the spindle in HeLa cells. It is followed by symmetric division where the cortical pull plays a key role [37]. Similar spindle localization at the cell center is also observed in *C. elegans* embryo during early prophase [38]. In *C. neoformans*, the spindle is formed and stabilizes near the septin ring within the daughter bud [16] (Fig 1, S1 Fig, S1 Video). The event is preceded by the migration of the nucleus [16, 39] as determined from the statistics in S1 Fig. Timely nuclear migration into the daughter bud requires directed force generation toward the daughter bud. Since, the proper positioning of the spindle and its alignment are crucial determinants of the faithful

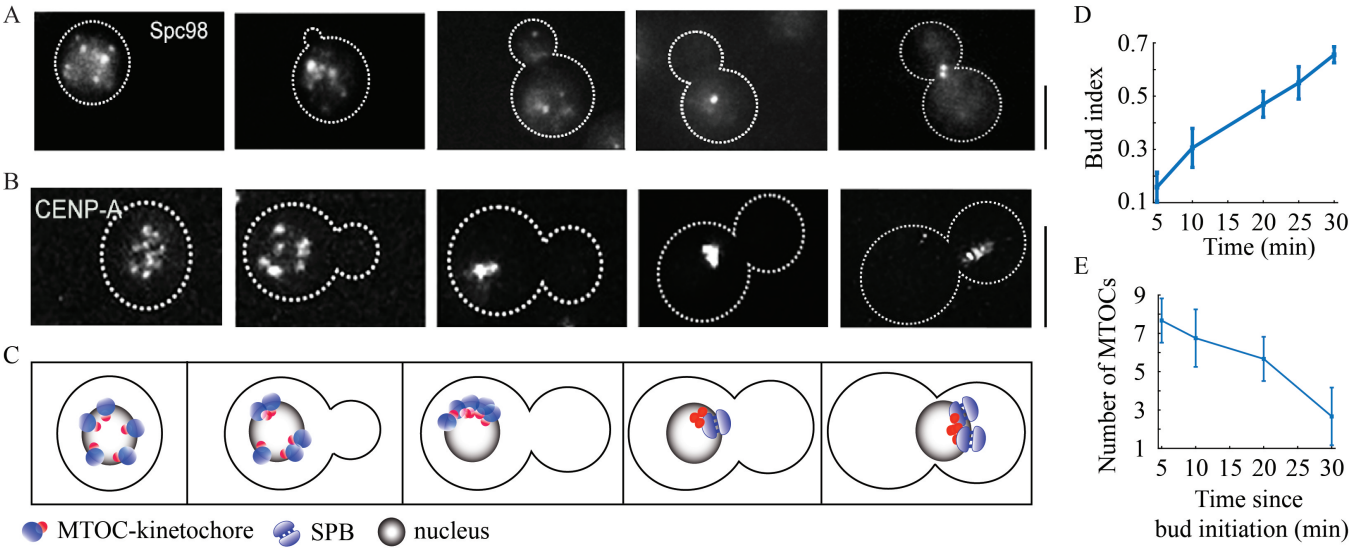

Fig 2. Clustering of MTOCs and KTs during mitosis in *C. neoformans*. Images of cells showing the localization of (A) Spindle pole body protein, Spc98, and (B) KT marker CENP-A at different stages of the cell cycle in the wild-type cells. Bar, 5 μm. (C) Schematic depicting the concomitant happening of the processes shown in (A) and (B). (D) Progression of bud growth with time. (E) Number of MTOCs in the cell as a function of time estimated from the bud size.

nuclear segregation [14, 39], the stable spindle localization near the septin ring inside the daughter bud [16] (Fig 1, S1 Fig, S1 Video) poses a natural question: what are the force balance conditions necessary for such localization?

In experiments, it is challenging to quantitatively estimate or tweak forces on the spindle in *C. neoformans*. Thus, modeling has been used to supplement/explain the experiments concerning various aspects of spindle mechanics [16, 40–48]. Previously, force balance models have been used to replicate the observed aspects of spindle dynamics [49–52]. The 'closest to experiment' approach would be to design simulation using an agent-based model [14, 16, 42, 44, 47, 48, 53], where all objects (e.g. MTs, motors, and other organelles) are simulated as agents having their movements dictated by laws of mechanics.

In this study, we utilized an agent-based model with MTs, MTOCs, and nucleus simulated as agents obeying laws of mechanics within a typical budded cell geometry (Fig 3A) [14, 16]. Despite the enormous advantages of such an agent-based model, it has certain limitations. In general, the possible number of molecular motors' combinations in various locations of the spindle at different cell cycle stages is too great (discussed in [54]) and far from clear, particularly in *C. neoformans*. The exact mechanics of the collective motor activity is significantly complex and yet to be well understood. Therefore, for simplicity, we chose not to simulate the molecular motors explicitly. Rather we opted for a description with constant motor densities where a particular motor-driven force on a MT is proportional to the predetermined motor density. To have a better understanding of the spindle positioning, we also set up a simple one-dimensional analytical model with closed-form expressions for various averaged forces (Fig 3B-3C). By screening these forces, we estimate the plausible force balance for proper spindle positioning in a confinement mimicking a budded cell [36, 49, 55]. These two models not only complement the primary experimental observations of spindle localization in *C. neoformans*, but reasonably corroborates with each other in a qualitative manner. In other words, the benchmarking of the analytical model is supported by the agent-based model and vice versa. Overall, our study highlights that several mechanistic processes can facilitate efficient clustering of MTOCs, either independently or in harness with the other. Furthermore, screening the outputs of *in silico* models uncovers that proper spindle positioning near the septin ring requires MT buckling from the cell cortex in *C. neoformans*.

Results

Developing *in silico* modeling framework

Computational Modeling: We consider the spindle dynamics occurring inside cellular confinement mimicking a budded cell (Fig 3A). The mother bud size (radius R_M) is fixed whereas the daughter bud (radius r_D) grows with time. Prior to the SPB formation, all the MTOCs (spheres of radii $r_{MTOC} \sim 0.1$ μm) are located on the surface of the outer NE (non-deforming spherical nucleus of radius r_{nuc}) and nucleate cMTs. The movement of the MTOCs is constrained on the surface of the NE. At the onset of the simulation, we considered 14 MTOCs [16, 26]. Each MT is modeled as a cylinder of zero thickness with its length regulated by four dynamic instability parameters (Table 1): catastrophe and rescue frequency (f_c, f_r); growth and shrinkage velocity (v_g, v_s). After complete clustering of MTOCs into the SPB and SPB duplication (Fig 2A-2E, 3A), the nMTs from both the SPBs grow inside the chromosomal volume and catch KTs. Meanwhile, the cMTs that reach the cell cortex, majorly experience instantaneous cortical push ($\vec{F}^{cell-mem}_{push-inst}$), push due to buckling against cell membrane ($\vec{F}^{buckle}_{cor}$), cortical dynein mediated pull ($\vec{F}^{dyn}_{cor}$) and Bim1 mediated bias towards septin ring ($\vec{F}^{Bim1}_{cor}$) (Fig 3A, S2 Fig A-S2 Fig C). Note that the +TIP protein Kar9 binds to the type 5 myosin Myo2 and the kinesin Kip3. Kar9 plays a significant role in early (pre-anaphase) spindle positioning, possibly by forming Bim1–Kar9–Myo2 complexes in *S. cerevisiae* [39, 56–60]. But, it has been reported

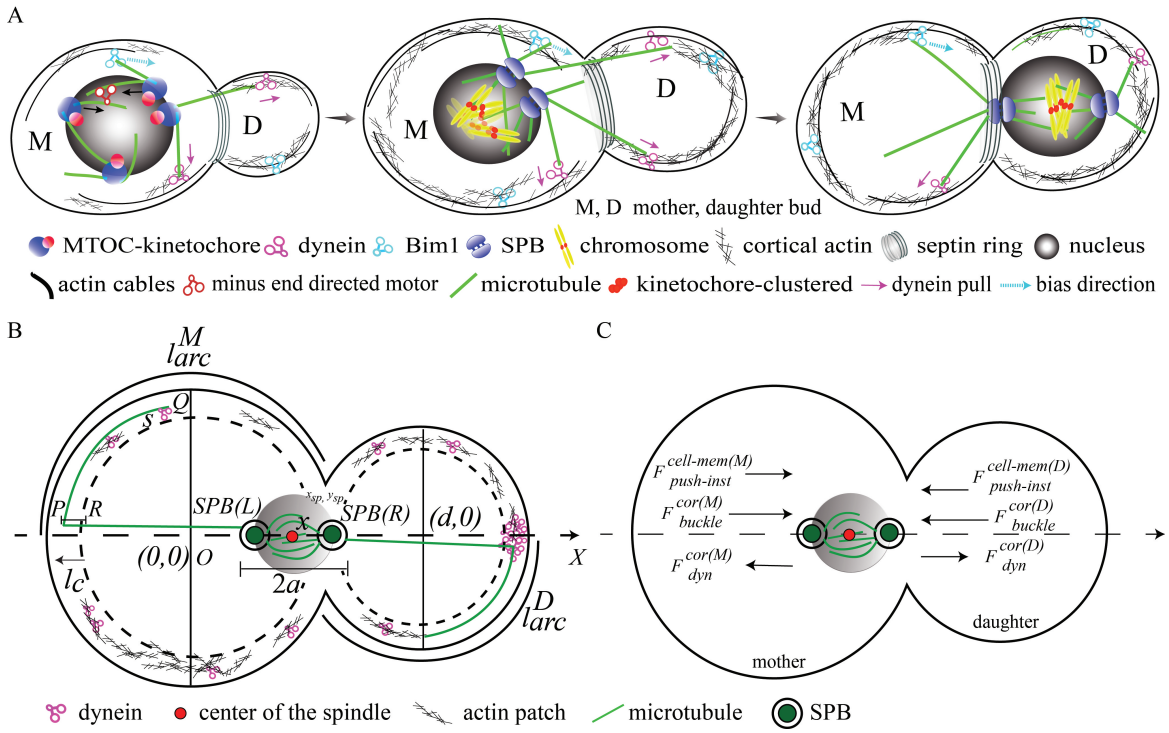

Fig 3. Representative schematic diagrams illustrating the computational and mathematical model. (A) Model schematic depicts the cell cycle stages in *C. neoformans* which are simulated utilizing the computational model. Plausible interaction of cMTs with the cell cortex and on the nuclear envelope are shown. Arrows indicate the direction of forces. (B) Schematic of the one-dimensional mathematical model for spindle positioning in *C. neoformans*. The origin $O(0,0)$ is located at the center of the mother bud while the center of the daughter bud is located on the axis of symmetry (namely the X axis) at $(d,0)$. The instantaneous position of the spindle is denoted by x measured from the origin. l_c denotes the width of the cortex, filled with mesh-like actins and dyneins. $SPB(L)$ and $SPB(R)$ denote the leftward and rightward SPBs and the green lines represent microtubules. In the mother bud, the section 'PR' is the 'uncurled' MT segment in the cortical region, and the segment 'PQ' denotes the 'curled' MT segment undergoing sliding within the mother cortex where cortical dyneins pull on both the segments. A similar interaction occurs in the daughter cortex as well. Localized cortical dynein patch in the daughter cortex around the axis of symmetry signifies the differential spatial distribution of dynein in the mother and daughter bud [16]. (C) The direction of the forces acting on the spindle in the mathematical model.

previously that the *C. neoformans* genome lacks a clear homolog of Kar9 [61]. In the absence of Kar9, we probed for the function of Bim1 (which is a +TIP protein and interacts with Kar9) in generating an effective cortical bias at the plus-ends of the cMTs [16]. To that effect, we noted the effective bias towards the septin ring as Bim1 mediated bias/force. Further, the cMTs grazing along the NE experience additional forces (S2 Fig D-S2 Fig E); one of them is $\vec{f}_{overlap}$ at the MT-MT overlap on NE. The $\vec{f}_{overlap}$ is proportional to the mean number of minus end-directed motors per unit length (λ_{ovl}) at the overlap (S2 Fig E). Similarly, forces between KTs and nMTs have been computed (for details, see Material and Methods). The instantaneous positions of all the objects (nucleus, MTOCs, SPBs, KTs) are updated by solving corresponding Stokes equations (Eq. 1-4 in Materials and Methods).

Mathematical Modeling: We formulated a mathematical model to study spindle positioning. We frame the mother and the daughter bud as two intersecting circles of radii R_M and r_D respectively (Table 1). The center of the daughter bud is chosen to be 'd' distance away from the center of the mother. In this framework, the spatial movement of the spindle is allowed along the line joining the centers, regarded as the axis of symmetry. For simplicity, our analytical model is one-dimensional where all the forces are projected along the axis of symmetry, namely the 'X' axis (Fig 3B-3C). The spindle is chosen to be a rigid rod of length $2a$ with two perfectly bioriented SPBs at its ends lying on the X-axis. We further assume that the cMTs from the SPB facing the mother (daughter) bud cell cortex namely $SPB(L)$ ($SPB(R)$), interact solely with the mother (daughter) bud cell cortex (Fig 3B-3C). In the following, we discuss the reasons behind these assumptions. The spindle is found nearly aligned with the axis joining the mother and daughter bud center (Fig 1). The geometric obstruction imposed by the solid nucleus, the relatively smaller aperture of the bud-neck junction, and the spindle alignment almost parallel to the axis joining the mother and daughter bud center prevent the cMTs from a SPB to interact with both mother and daughter bud cell cortex in an isotropic manner. The cMTs emanating from the SPB facing the mother (daughter) bud cell cortex majorly interacts with the mother (daughter) cell cortex only (Fig 3A).

Further, in the model, we considered exponentially decaying spatial dependence of forces, a straightforward and widely used choice [36, 49, 55]. We derived closed-form expressions for various MT-mediated forces (instantaneous cortical push, cortical dynein pull, the force due to MT buckling) on the spindle due to MT-cell cortex interaction. The sum of all these forces accounts for the total force on the spindle. The net force balance on the spindle (rigid rod constituting $SPB(L)$ and $SPB(R)$) determines the spindle position.

Here, the strength of dynein-mediated pulling is regulated by λ^M_{dyn} (Eq. 7-8 in Materials and Methods) and λ^D_{dyn} (Eq. 10-11 in Materials and Methods), cortical pushing by A_M and A_D (Eq. 5 and Eq. 6 in Materials and Methods), average MT length by L^{av}_{MT} (Eq. 5-8, Eq. 10-11, Eq. 13-14 in Materials and Methods). In the numerical simulation, the corresponding model parameters are adjusted according to the values listed in Table 1. In most of the cases, the choice of the parameter values is based on the earlier published reports. However, due to the paucity of exact numbers in the literature, a few of the chosen parameter values are optimized for the current study through sensitivity analysis. Below, we present the model investigations exploring MTOC clustering and spindle positioning in *C. neoformans*.

Clustering of MTOCs progresses via redundant pathways

We have shown previously that all KTs cluster to form a punctum in $\sim$ 25 mins [16]. We further demonstrated that KTs colocalize with MTOCs [25]. Now, we validated the time required for MTOCs to coalesce into an SPB by calibrating the clustering time since bud initiation (time set to zero), in terms of the budding index (Fig 2D-2E). We observed that since the bud initiation, the daughter bud grows with time in a reasonably uniform manner over a large population of cells. As the bud growth rate is roughly consistent, the budding index can be thought of as an intrinsic 'clock' of a budded cell (Fig 2D). The number of MTOCs in cells having similar budding indices (implying that the cells are at the same cell cycle stage) were counted and plotted with 'time' (calibrated from the budding index) to estimate the MTOC clustering time (Fig 2E). We observed that the timescale for KT clustering [16] and MTOC clustering (Fig 2E) are similar ($\sim$ 25 min) and in reasonable synchrony with each other (Fig 1, 2A-2C). Although electron microscopy suggested as many as 14-16 MTOCs [26], with a limited resolution we could identify a maximum of 8-10 MTOCs in small budded cells.

Next, we address the question of how all the MTOCs cluster into a single group within this specific timescale using an agent-based mechanistic model (Fig 3A, 4A, S2 Fig). First, we investigated the MTOC clustering process via MT driven 'grow-and-catch' ('search and capture') on the NE without the cortical interactions (Fig 4A, S2 Fig D-S2 Fig E). To begin with, we determined the time required for all the MTOCs to cluster if cMTs growing out of MTOCs slide along the NE and directly catch the MTOCs (S2 Fig D). We considered that in the 'direct grow and catch' mechanism (Fig 4A, S2 Fig D), the MTs contributing to the clustering process remain confined to the

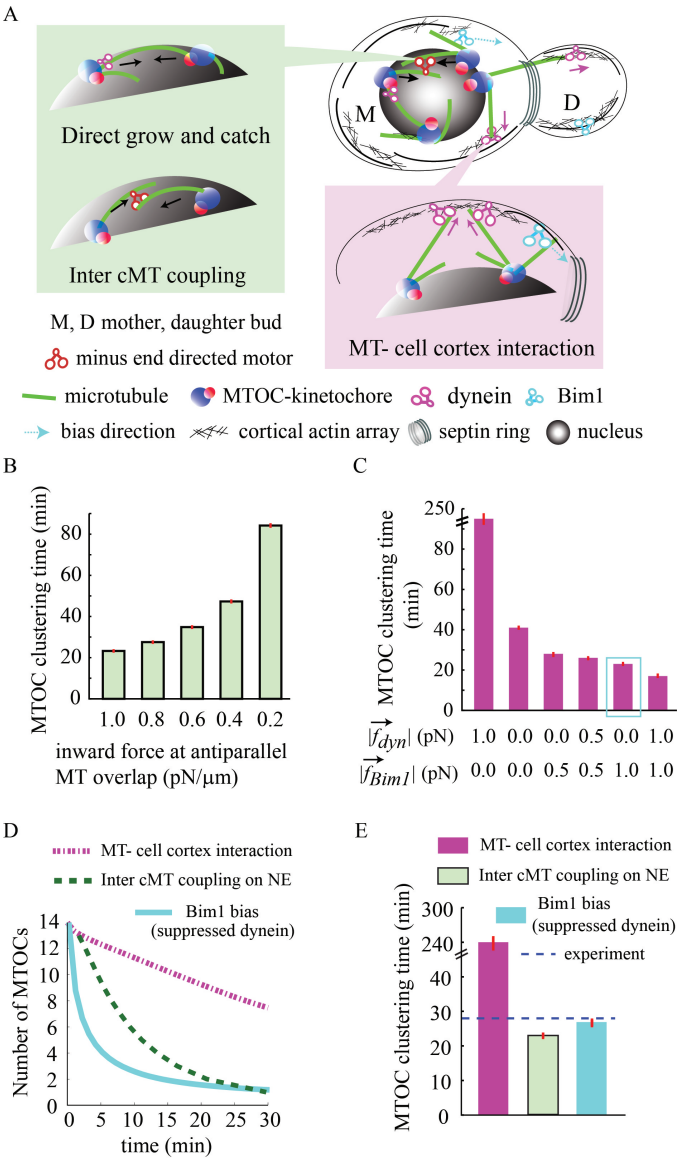

Fig 4. Cooperative interactions among MTs and motors govern MTOC clustering. (A) Model schematic depicting MT-mediated grow-and-catch ('search and capture') processes and forces required for the clustering of MTOCs. Arrows indicate the direction of forces. Plausible clustering mechanisms illustrated are: a growing cMT directly catching an MTOC ('direct grow-and-catch'), sliding of anti-parallel cMTs via crosslinking minus end-directed motors on the NE (inter cMT coupling at the NE), and cMT plus-ends interacting with cell cortex (MT-cortex interaction). (B) Clustering time in the sole presence of inter cMT coupling at the NE increases as the minus-ended motor-generated inward force at MT-MT overlap decreases. The MT number is fixed at 4 per MTOC. (C) Clustering solely via MT-cell cortex interaction. The clustering is faster when Bim1 bias is enhanced. $|\vec{f}_{dyn}|$ ($|\vec{f}_{Bim1}|$) represents the magnitude of the force generated by a single dynein (Bim1) on each MT at mother cortex. (D) Time progression of MTOC clustering in different mechanisms. The first/fifth bar in Fig 4C denotes the parameter values corresponding to the magenta/cyan curve in Fig 4D respectively. (E) Comparison between MTOC clustering timescales via MT-cell cortex interaction, inter cMT coupling on NE and Bim1 bias with suppressed dynein activity at cell cortex ($|\vec{f}_{dyn}| = 0.0$ pN, $|\vec{f}_{Bim1}| = 0.5$ pN). In all figures, sample size n>2000 for simulation and red bars indicate SEM (wherever shown).

Table 1. List of parameters chosen for the model analysis

Abbreviation	Meaning	Value	Reference
R_M	Radius of the mother bud	3 μm	[16]
r_D	Radius of the daughter bud	0.0-2.15 μm	[16]
r_{nuc}	Radius of the nucleus	1.0 μm	[16]
r_{SPB}	Radius of single SPB	0.125 μm	[62,63]
k_{cor}	Spring constant of the cortex	5.0 pN/μm	[14,64]
η_{cyt}	Viscosity of cytoplasm	5.0 pN s/μm^2	[14,64]
η_{nu}	Viscosity of nucleoplasm	10.0 pN s/μm^2	[14,64]
η_{NE}	Effective viscosity of NE	10-15 pN s/μm^2	[14,64]
v_g	MT growth velocity	10.4 μm min^{-1}	[16,65,66]
v_s	MT shrinkage velocity	28.6 μm min^{-1}	[16,65,66]
f_c	Catastrophe frequency of MT	1.0 min^{-1}	[16,65,66]
f_r	Rescue frequency of MT	0.02 min^{-1}	[16,65,66]
f_c^{stall}	Catastrophe rate of stalled MT	0.04 s^{-1}	[67]
f_{stall}	MT stall force	1.7 pN	[68]
f_{dyn}	Force produced by single dynein	1.0 pN	[69,70]
f_{Bim1}	Force produced by single Bim1	1.0 pN	[16]
$\lambda_{dyn}^{M(D)}$	Number of dyneins per unit length per MT	6.0 /μm	[71]
λ_{ipMT}	Number of ipMT motors per unit length per MT	1.0 /μm	[64]
λ_{dyn}^{ovl}	Number of minus ended motors per unit length at NE	1.0 /μm	This study
$f_{kinesin-5}$	Force produced by single kinesin-5 motor	1.0 pN	[14]
$K_{cohesin}$	Spring constant of the cohesion springs	0.1 pN/μm	[72]
K_c	Spring constant of KT-kMT connection springs	10.0 pN/μm	[64,73]
K_{fibril}	Spring constant of the KT fibril	5.0 pN/μm	[64,73]
D_{buckle}	Buckling amplitude per MT	200.0 pN μm^2	[55]
	Additional parameters for analytical model		
A_M (A_D)	Instantaneous cortical push amplitude at mother(daughter)	5 pN	This study
B_M (B_D)	Cortical pull amplitude at mother(daughter)	5 pN	This study
D_M (D_D)	Buckling amplitude at mother(daughter)	1000 pN μm^2	[55], this study
C_M (C_D)	Steric repulsion amplitude at mother(daughter)	10 pN	[55], this study
ζ_M (ζ_D)	Range of steric repulsion at mother(daughter)	1000	[55], this study
L_{MT}^{av}	Average cMT length	10 μm	This study
a	Spindle half length	1.0 μm	This study
r_D	Radius of the daughter bud	2.15 μm	This study
l_c	Cortex width	0.2 μm	[14,74]

NE while growing in a random direction. As the 'searcher' MT tip nucleated from an MTOC grazes along the NE and 'catches' another MTOC ('target'), the MTOCs move toward each other along the MT until they fuse ((Fig 4A, S2 Fig D)). The movement of the MTOCs is strictly restricted to the NE. In this context, we assumed a fixed number of grazing cMTs per MTOC ($\sim$ 3-4 cMTs per MTOC). We found that, in the explored parameter regime, the timescale for complete clustering achieved by this 'direct grow-and-catch' pathway is significantly large surpassing the relevant mitotic timescales. The MTOCs take $\sim$ 1.5 h to cluster entirely, that too, in $\sim$ 10 % of the cell population only. The MTOCs fail to cluster into a single focus, in the rest of the cell population even after $\sim$ 4-5 hr. Note that, in the current *in silico* study, the term 'cell population' alludes to the total number of independent simulation runs started with uncorrelated initial configurations. In this particular context, we performed many independent simulation runs and in 10 % of these simulations, clustering less than 1.5 h was observed. Thus, in the currently explored parameter regime, it is unlikely to be an 'efficient' pathway for MTOC clustering. However, the possibility that the same pathway functioning efficiently in combination with other pathways cannot be ruled out.

Next, we introduced antiparallel sliding amongst the grazing cMTs on the NE (inter cMT coupling, Fig 4A, S2 Fig E). Inward sliding of the overlapping cMTs from two different MTOCs can be steered by crosslinking minus end-directed motors [75]. The crosslinking activity of minus end-directed motors acting at the MT-MT overlap brings

the engaged MTOCs towards each other. In the earlier scenario, a 'searcher' MT has to grow and catch another MTOC. However, in the present context, a 'searcher' MT can grow and catch another MT segment so that the minus end-directed motors can crosslink them and initiate antiparallel sliding. Adding the minus end-directed motor crosslinking and sliding on the NE facilitate the timely clustering; clustering of all the MTOCs ($\sim$ 100 %) into a single object happens within $\sim$ 23 min (Fig 4B, S2 Video). As expected, when the inward force between the MTOCs due to minus ended motors diminishes, the net clustering time increases (Fig 4B). Additional parameter sensitivity analysis for this clustering mechanism is described in S1 Text, S3 Fig.

Next, we explore the role of cMT-cell cortex interaction leading to the clustering of the MTOCs. Two major cortex-based forces on the cMTs are: (a) net pull on the MT segments sliding inside the cortex via the cortical dyneins towards the cortex; (b) Bim1 mediated force on the cMTs (sliding +ve end of the cMTs along the cortex) having a directional preference towards the septin ring (MT-cell cortex interaction, Fig 4A, S2 Fig A-S2 Fig B). We found that the exclusive activity of dynein mediated MT-cell cortex interaction leads to nearly complete clustering of the MTOCs, but the time estimated ($\sim$ 240 min) is way too high (Fig 4C, S3 Video). However, a decrease in the cortical pull and/or subsequent increase in the Bim1 mediated bias reduces the clustering time scale to $\lesssim$ 50 min (Fig 4C, 4D, S4 Video). We find that the dynein mediated pull on the MTOCs via cMTs acts in random directions, whereas the Bim1 mediated bias is directed towards the septin ring. Thus dynein dominated cortical pull suppresses the effective Bim1-bias and delays the clustering. When dyneins are suppressed, due to Bim1-bias all the MTOCs are drifted towards the septin ring along the NE and cluster rapidly. Note that, if the clustering time via a mechanism largely exceeds the physiological time limit estimated from the live-cell imaging, the sole presence of the mechanism under consideration may be discarded. In reality, in the context of a dividing cell, significantly delayed clustering by any 'inefficient' mechanism is unlikely to happen.

The time scales for complete MTOC clustering appears to be similar and close to the physiological time limit when, (a) MTOCs aggregate due to antiparallel sliding of the grazing MTs on the NE via minus ended motors and (b) MTOCs aggregate due to diminished cortical dynein pull concomitantly with enhanced Bim1-bias at the cortex (Fig 4D, 4E, Table 2). This highlights an important physical possibility that the clustering mechanisms may be redundant, i.e., the mechanisms either act in liaison or independently.

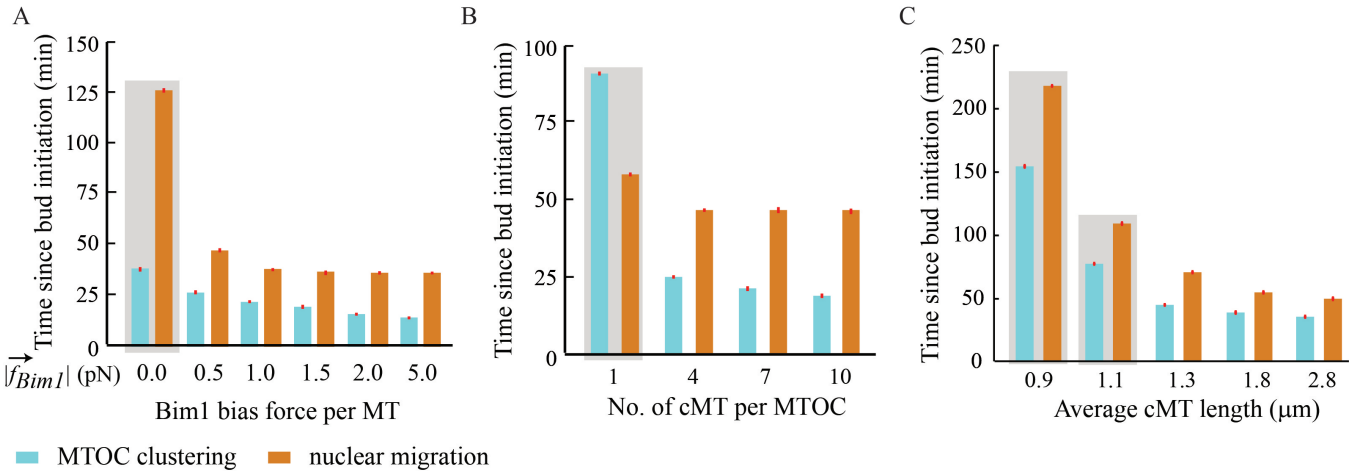

Fig 5. MTOC clustering and nuclear migration: sensitivity to model parameters. (A-C) Time required for complete MTOC clustering and proper nuclear migration to daughter bud when Bim1 bias force per MT (A), number of MT per MTOC (B) and average cMT length (C) are varied. For MTOC clustering, solely the mechanism of "MT-cell cortex interaction with diminished cortical pull and enhanced Bim1 bias" is considered. In all figures, sample size n>2000 for simulation and red bars indicate SEM (wherever shown).

The complete clustering of MTOCs into a single body marks the formation of the mature SPB followed by SPB duplication. Subsequently, the duplicated SPBs separate into a bi-oriented configuration that initiates spindle formation. In our earlier and present studies, it has been shown that the mitotic spindle stabilizes inside the daughter bud close to the septin ring in *C. neoformans* [16] (Fig 1, S1 Video, 3A).

Therefore, an obvious precursor to the spindle positioning inside the daughter bud is nuclear migration from the mother bud to the daughter. From a mechanistic standpoint, this is facilitated by cortical interaction of cMTs (Fig

Table 2. Various mechanisms of MTOC clustering as examined by the *in silico* model

Interaction mechanism	Clustering time (min)	% of MTOCs clustered within 25 min
cMT-cell cortex interaction	~ 240	~ 40
Inter cMT coupling at the NE	~ 23	~ 100
cMT-cell cortex interaction with diminished cortical pull and enhanced Bim1 bias	~ 25 [16]	~ 99

3A, S2 Fig A-S2 Fig C) [14, 16]. Interestingly, cortical interaction is also an important mode of MTOC clustering as we have already shown. Therefore, MTOC clustering, nuclear migration, and subsequent positioning of the spindle are the sequence of crucial mitotic events which are unlikely to be mutually exclusive. The key elements necessary for orchestrating the pre-anaphase MTOC clustering and nuclear migration are: (a) MT integrity, (b) spatiotemporal localization and activity of Bim1 and dynein [16]. Bim1 and dynein, majorly generate the forces which are transduced via cMTs to the MTOCs (later SPBs) and the nucleus.

Previously, we showed that Aurora B kinase Ipl1 in *C. neoformans* plays a pivotal role in (a) maintaining MT stability and (b) regulating Bim1/dynein activity or localization [16]. Therefore, the depletion of Ipl1 would interrupt both MT stability and Bim1/dynein activity. In that scenario, we observe that delayed KT clustering resulted in delayed nuclear migration S4 Fig. Since the time scales of MTOC clustering and KT clustering are similar and they occur concomitantly [16] (Fig 2A-2E), it is likely that delay in MTOC clustering also leads to a delay in nuclear migration.

Taking cues from these experimental observations, we asked the following questions in the *in silico* model: (a) What happens to the nuclear migration and concomitantly progressing MTOC clustering when cortical Bim1 and dynein densities are varied? Note that, 'density' of molecular motors and 'force' applied by them are proportional in our model. Thus, variations in the Bim1 and dynein densities allude to equivalent variations in the respective forces. (b) Does impaired/delayed clustering lead to faulty migration? (c) What happens to the spindle positioning and spindle orientation when MTOC clustering is delayed?

To address these questions, we carried out sensitivity analysis over the following parameters: Bim1 bias force per MT, the number of MT per MTOC, and average cMT length (Fig 5A-5C, S5 Fig A-S5 Fig B). We find that the time required for MTOC clustering and nuclear migration are reasonably correlated. If the MTOC clustering is delayed/accelerated, nuclear migration also follows a proportional timescale (Fig 5A-5C) [16].

Interestingly, the *in silico* analysis further suggests that the delay in nuclear migration and MTOC clustering do not affect the spindle positioning or the spindle orientation in the currently explored parameter regime (S5 Fig A-S5 Fig B). Variations in Bim1 bias force per MT and the number of MT per MTOC incur variations in the nuclear migration time (and MTOC clustering time) within a reasonable range (Fig 5A-5C). But the spindle positioning within the daughter bud (and spindle orientation) turns out to be independent of the variations in Bim1 bias force per MT and number of MT per MTOC (S5 Fig A-S5 Fig B). In other words, irrespective of whether the nuclear migration is delayed or accelerated, the stable spindle position (and spindle orientation) remain unchanged within this specific cellular geometry (S5 Fig A-S5 Fig B). Experimental quantification of various spindle attributes in wild-type and upon molecular perturbations (S1 Fig, S5 Fig C-S5 Fig E, S6 Fig) are discussed in the following sections.

To understand the stable spindle localization, we propose a simple analytical model that estimates net force balance on the spindle (See Materials and Methods, S1 Text, 3B-3C). We considered closed-form expressions for various MT-based forces and examined possibilities of the spindle localization under the combinatory effect of these forces (Fig 3, 6, S7 Fig).

Balance of cellular mechanical forces guides the spindle position

A spindle is constantly acted upon by molecular forces arising from the interactions of its components with the surrounding [14, 16, 36, 43, 48, 64, 76, 77], e.g., cMTs interacting with the cell cortex via dynein generates a pull on the nucleus toward the cell periphery; similarly, cMTs buckling in contact with the cell membrane pushes the nucleus

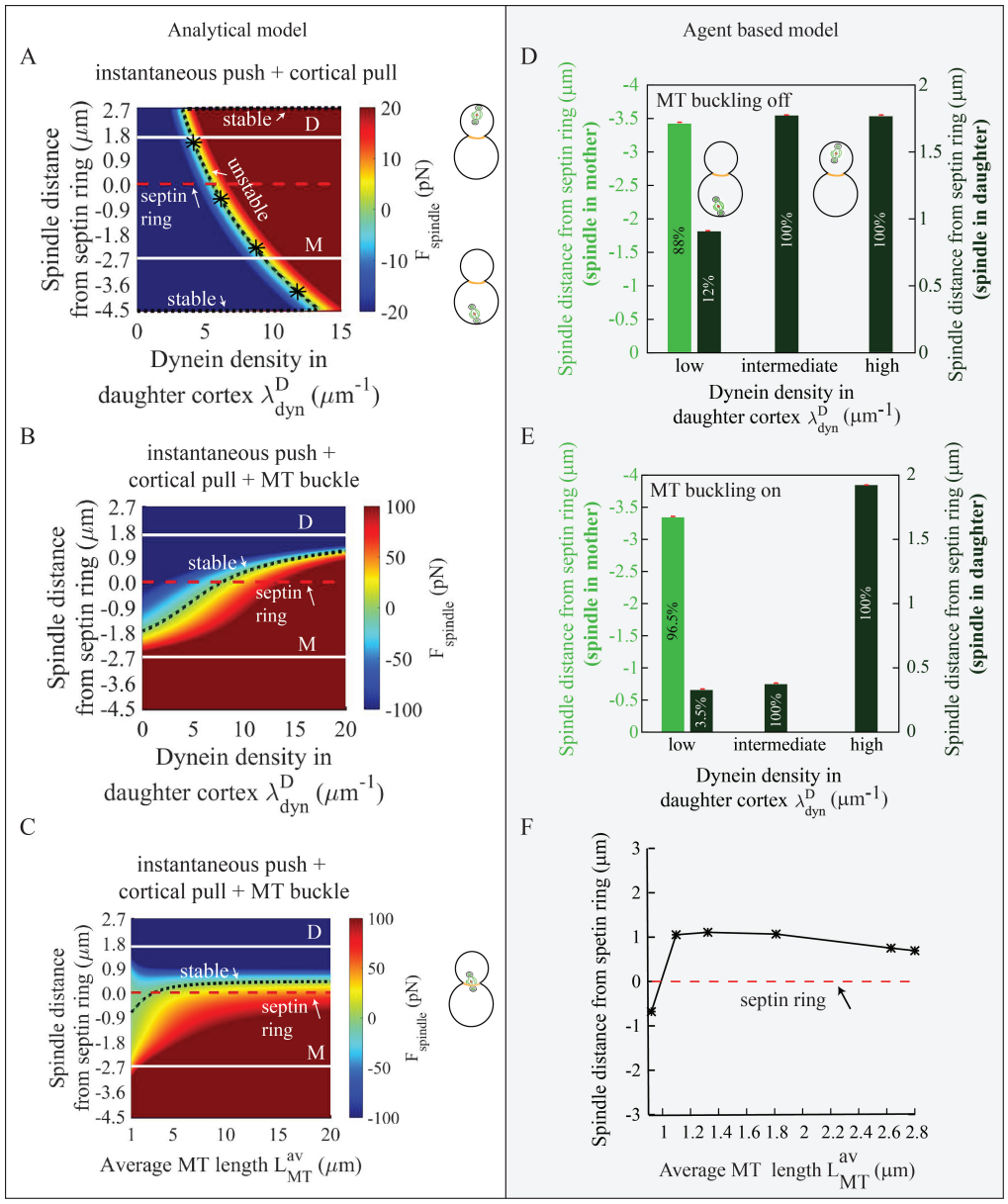

Fig 6. The mechanistic models of force balance explain spindle positioning in *C. neoformans*. (A) Spindle stably collapses onto the cell cortex as dynein density in the daughter cortex (λ^{D}_{dyn}) is varied. Dynein density in the mother cortex (λ^{M}_{dyn}) is fixed and instantaneous cortical push is present in both mother and daughter cortex. Color bars represent the net force on the spindle and white solid lines denote the center of the daughter and mother buds. (B-C) MT buckling is present combined with instantaneous push and cortical pull. Increasing dynein density in the daughter cortex (λ^{D}_{dyn}) steadily brings the spindle into the daughter, localizing near the septin ring (B). Spindle position varies depending on the average MT length L^{av}_{MT} (C). (D-E) Spindle distance from septin ring in the absence (D) or presence (E) of MT buckling at the cortex as observed in the agent-based simulation. The values within the bars indicate the percentage of spindles in mother or daughter, across the cell population. (F) Spindle position depending on the variation in average MT length (L^{av}_{MT}) as observed in agent-based simulation when instantaneous cortical push, dynein pull, and MT buckling are acting in tandem. In plots A-F, -ve/+ve distance refers to the spindle in mother (M)/daughter (D) bud.

away from the membrane. These interactions are plausible in both mother and daughter bud cell cortices. Besides, interactions of cMTs with the septin ring and the cortical actin cables generate an effective bias translating the plus ends of the cMTs toward the daughter bud. Since these forces are spatially inhomogeneous and rapidly varying with time, it is logical to ask how the nucleus and the spindle attain steady positions before the chromosomal segregation.

We formulate an analytical template in one-dimension that accommodates key MT-mediated forces originating from the mother and daughter cortices acting on the SPBs (Fig 3B-3C). The mechanistic force balance landscape emerging from the mathematical model allows us to carry out sensitivity analysis across a wide parameter regime constituting a myriad of forces with different characteristics (e.g. instantaneous pushing and buckling of the cMTs, dynein mediated pulling, etc.). From experiments and agent-based simulation, we observe that the average spindle length is ~ 1.5 μm in wild-type (S5 Fig C) and the neck to spindle distance is ~ 1 μm while the spindle is in the daughter bud (S5 Fig D). Also, the spindle lies almost parallel to the axis of symmetry (orientation angle ~ 15 degree) joining the centers of mother-daughter bud (S5 Fig E).

To test how sensitive is the spindle positioning to the cMT-cortex based forces, we introduced instantaneous push and dynein pull from both the mother and daughter cortex. Then, we varied the dynein density in the daughter cortex, keeping the rest of the parameters fixed at base values denoted in Table 1. If the dynein pull from the daughter cortex is too strong, the spindle collapses onto the daughter cortex. In the other limit, the spindle collapses onto the mother cortex, when the cortical pull from the mother cortex overpowers the pull from the daughter (Fig 6A). Thus, in the absence of MT buckling, the spindle localizes at the cortex. Note that here the term 'collapse' means the spindle is dragged too close to the cell cortex.

Adding the force due to MT buckling (with two other forces: cortical pull and instantaneous push) restores the stable spindle position near the septin ring (Fig 6B-6C). The spindle robustly maintains its position inside the daughter bud, close to the septin ring upon considerable variation in the average cMT length (Fig 6C, Table 3).

We also tested the spindle positioning in the absence and presence of MT buckling exploiting the three-dimensional agent-based computational model (Fig 6D-6E). We find that a moderate dynein pull is crucial for the spindle to migrate into the daughter. In the absence of MT buckling, the spindle localizes deep inside the daughter cortex for moderate and strong dynein pull from the daughter (Fig 6D). For low values of dynein pull from the daughter cortex, the nucleus is retained in the mother bud (Fig 6D). In the experiment, we observe that upon dynein depletion most of the cells have nuclei retained in the mother bud (S6 Fig A) which is in agreement with the model outcome (Fig 6D). Deletion of Bim1 also leads to faulty nuclear migration (Fig 5A, S6 Fig B). While acquiring the statistics in S1 Fig, S6 Fig A-B, we have only considered reasonably large budded cells having bud indices 0.65 and above. Since the bud index is an indicator of 'time' (Fig 2D), higher bud indices refer to the cells in which a considerable amount of time has elapsed after bud initiation. In most of the wild-type cells with bud indices above 0.65, the nuclei are settled in the daughter bud (S1 Fig). Upon dynein depletion/Bim1 deletion, we observe more cells with bud indices above 0.65 have nuclei retained in the mother bud (S6 Fig A-B) because in those cells, the nuclear migration is possibly delayed/impaired.

However, with MT buckling turned 'on', the spindle settles inside the daughter bud and stabilizes close to the septin ring in the currently explored parameter regime (Fig 6E).

As the mechanics of spindle positioning is largely MT mediated [16, 36, 39], we tested the dependence of spindle positioning on the average MT length. From the analytical and the agent-based model analysis, we found that when the average MT length is 'too short' (~ 1 μm), the spindle is retained in the mother (Fig 6C, 6F). In other words, the nucleus is unable to migrate to the daughter bud. This result corroborates with our experimental observations (S6 Fig C-D). We observe spindle localization inside the daughter bud near the septin ring in wild-type cells (Fig 1, S6 Fig C, S1 Video). But in cells treated with nocodazole, the MT integrity is severely compromised (S6 Fig D). In that scenario, we do not observe any spindle localization in the daughter bud (S6 Fig D).

We further observe that in the presence of MT buckling, the variation in average MT length above a threshold does not affect the spindle localization inside the daughter bud (Fig 6C, 6F). As a plausible explanation, we argue that when the average cMT length is above a threshold, a few cMTs always reach the cortex. At the cortex, interaction of MT and molecular motors transduce forces of pN order which is sufficient to stabilize the spindle at the proper location. Nevertheless, the force due to the buckling of a MT is considerably large compared to other relevant forces (Table 1). Therefore, the buckling transition of only a few cMTs from the cortex produces sufficient forces dominating the spindle localization. The position of the spindle remains unaffected because (a) the buckling mediated forces pointing away from the mother and daughter bud cell cortex are oppositely directed (Fig 3C), (b) number of MTs undergoing buckling at mother and daughter bud cell cortex are similar on average. Therefore, in the buckling

Table 3. Analysis of parameter sensitivity in spindle positioning (analytical model). M, D stand for mother and daughter bud respectively. * Spindle collapsed onto the cell cortex. The term 'collapse' means that the spindle is pulled to a very close proximity of the cell cortex. † Below/above this particular value of dynein density, spindle jumps sharply to the stable point at mother (daughter) bud cell cortex from stable point at daughter (mother) bud cell cortex with no unstable point in between the crossover.

Instantaneous push	Cortical pull	MT buckle	Variation	Magnitude	Spindle position	Plot
✓(M,D)	✓(M,D)	✗(M,D)	λ_{dyn}^{D}	low intermediate high	M* (stable) M* (stable), D* (stable) & unstable points in between D* (stable)	Fig 6A
✓(M), ✗(D)	✓(M), ✗(D)	✗(M,D)	λ_{dyn}^{M}	low intermediate high	D* (stable) 'sharp' transition† M* (stable)	S7 Fig C
✗(M), ✓(D)	✗(M), ✓(D)	✗(M,D)	λ_{dyn}^{D}	low intermediate high	M* (stable) 'sharp' transition† D* (stable)	S7 Fig C
✓(M,D)	✓(M,D)	✗(M,D)	L_{MT}^{av}	low intermediate high	D* (stable), M* (stable) & unstable points in between " D* (stable)	S7 Fig E
✓(M), ✗(D)	✓(M), ✗(D)	✓(M), ✗(D)	λ_{dyn}^{M}	low intermediate high	D* (stable) stable transition from D to M M (stable, slightly away from the cell cortex)	S7 Fig F
✗(M), ✓(D)	✗(M), ✓(D)	✗(M), ✓(D)	λ_{dyn}^{D}	low intermediate high	M* (stable) stable transition from M to D D (stable, slightly away from the cell cortex)	S7 Fig F
✓(M), ✓(D)	✓(M), ✓(D)	✓(M), ✓(D)	L_{av}^{MT}	low intermediate high	M (stable) D(stable), **close to septin ring** "	Fig 6C

dominated landscape, the forces directed away from the mother and daughter cell cortex nullify each other near the septin ring.

To conclude, the spindle distance from the septin ring measured in the experiment (S5 Fig E) and estimated from the analytical (Fig 6C) and computational models (Fig 6F) reasonably agree with each other. Additional spindle characteristics predicted by the model are summarized in the S1 Text, S7 Fig, and Table 3.

Discussion

Our theoretical approach combines a) an agent-based computational model of MT 'grow-and-catch' ('search and capture'), and b) an analytical model to explore the mitotic events in *C. neoformans*. With the help of the computational model, we examined the role of MT grow-and-catch ('search and capture') during MTOC clustering, nuclear migration and spindle localization. Using the analytical model, we screened various combinations of the MT-based mechanistic forces and found out plausible mechanical force balance conditions that may orchestrate proper spindle positioning. We reached the following conclusions (Fig 7).

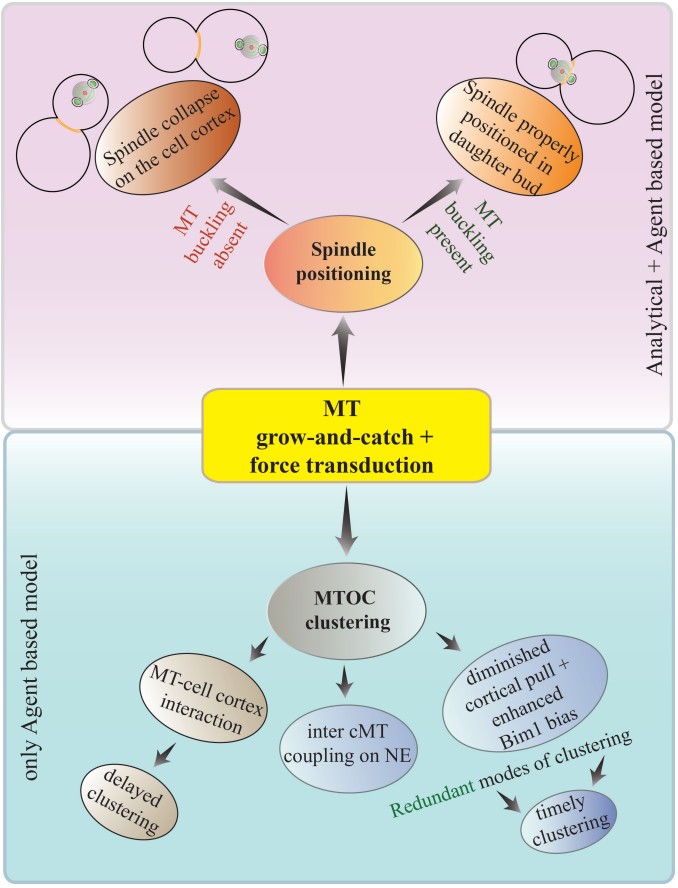

Fig 7. Summary of model outcomes describing mechanistic aspects of MTOC clustering and spindle positioning in *C. neoformans*. The agent-based model depicts redundant mechanisms for the timely clustering of MTOCs. Inter cMT coupling at NE and/or cortical interaction of MTs with suppressed dynein pull and enhanced Bim1 bias may facilitate timely clustering, either independently or in unison. Furthermore, the analytical model supported by agent-based simulations suggests that proper spindle positioning in the daughter bud near the septin ring requires MT buckling from the cell cortex.

The emergent time scales for MTOC clustering are similar in two scenarios; the design principles of which are based on a) effective inter-MTOC attraction due to minus end-directed motor crosslinking between grazing antiparallel MTs on the NE and b) effective drift of all the MTOCs towards the septin ring due to Bim1 mediated cortical bias with diminished dynein pull from the cortex. In the first scenario, the clustering time scales down with the minus end motor mediated inward force at the MT-MT overlap. In the latter one, the clustering time scales up with the net cortical dynein pull on the MTs. From a model perspective, the comparable timescales of these two independent clustering mechanisms indicate a possible redundancy between the two mechanisms (Fig 4D-4E).

During mitosis, cells self-organize the spindle to facilitate nuclear division and for a faithful division, it is important to have a bipolar spindle. The reason is that the sister chromatids require to partition into two opposite poles and settle in two daughter progeny. In mammalian cells, the prevalence of more than two centrosomes at the beginning of

mitosis can generally be linked to multipolar spindle formation [36]. Multipolar spindles and the presence of more than two centrosomes/MTOCs often lead to chromosome instability, aneuploidy, erroneous attachments of chromosomes, and various other defects of chromosome segregation hindering faithful division. Recent studies highlight an interesting pathway of bypassing these defects where multiple centrosomes/MTOCs assemble into two groups/poles making way for bipolar spindle formation in multi-centrosome/multi-MTOC cells. The process of converging multiple centrosomes into two poles during spindle formation is often termed as 'centrosome clustering' [36, 78–80].

However, in the context of MTOC clustering in *C. neoformans*, the pathway for grouping the MTOCs into two poles turns out to be different. In *C. neoformans* we observe that MTOCs, dynamically move toward each other along the surface of the outer NE and eventually fuse forming the SPB. During this process, KTs are found to colocalize with the MTOCs (Fig 2A-2C). Unlike centrosome clustering resulting in two independent poles, MTOCs cluster into a single pole. The clustered pole, namely the SPB, subsequently duplicates into two SPBs paving the way for bipolar spindle formation.

Our analytical model, by screening various MT-based forces, qualitatively highlights the mechanical requirements for proper spindle positioning. It has been suggested that the plane of mitotic division is defined by this stable positioning of the spindle inside the daughter bud with spindle orientation almost parallel to the axis joining the centers of the mother and daughter buds [14, 16, 81]. Our model shows that in the presence of two opposing forces, instantaneous cortical push and dynein pull (no MT buckling), the spindle collapses onto the cortex. Additional force due to MT buckling at the mother and daughter cortex is essential to restore the stable positioning of the spindle near the septin ring. A key reason is the force due to buckling that scales with the inverse square of the MT length. Thus, when the spindle is close to the cortex, buckling MTs strongly push it away preventing the collapse. The analytical model also shows several interesting positions of the spindle which are unstable. The one-dimension model, however, can be extended to higher dimensions which would include several important characteristic degrees of freedom (e.g. orientation of the spindle, the angular displacement of the SPBs, etc.) in the analysis as well.

To examine the physical basis and the consistency of the spindle positioning attributes, results from the analytical model are compared with the agent-based computational model. One of the basic differences between the analytical and computational models is the stochastic effects. The agent-based model entails stochastic fluctuations stemming from the MT dynamic instability, a finite number of MTs, motor activity, etc.; whereas the analytical model, does not contain stochastic fluctuations, as well as temporal degrees of freedom. Possibly, due to intrinsic fluctuations in the computational model, we do not observe any unstable spindle position.

In the agent-based model, a major source of fluctuations is the stochastic MT dynamics manifesting the random switch between the states of polymerization and depolymerization [1,82–84]. In the mathematical model, the stochastic MT dynamics is not explicitly considered; the MT length distribution is chosen to be exponential. In the agent-based model, stochasticity also comes into the picture through MT interaction with the cortex/cell membrane. When an MT elongates to the cortical region the consequence is a probabilistic choice of the MT a) undergoing catastrophe, b) sliding along the cortex, and c) buckling with the tip hinged/pivoted at the cell membrane. However, stochasticity stemming from the explicit binding or unbinding of the motors on MTs, collective 'walking' of various groups of motors on the filaments, and associated modulations in force transmission via the MTs are not explicitly incorporated in the coarse-grained model. The stochastic effects arising from the thermal fluctuation at the molecular level and interactions of the 'objects' with embedding viscous medium (e.g., the cytoplasm, the nucleoplasm) are not accounted for in the model.

Previously, the mechanics of MT aster positioning has been studied with considerable details, in various contexts [85–87]. It has been suggested that both pushing and pulling forces (primarily relative to the cell boundary) govern the force balance landscape necessary for MT aster positioning. The mechanical conditions for a stable centering position for an MT aster within a confined geometry are: (a) pushing forces in tandem with MT catastrophe in the cytoplasm before the MTs hit the cell boundary; (b) pulling forces in tandem with MT sliding/slippage at cell cortex [87]. In the context of *C. neoformans*, we observe that the stable spindle positioning near the septin ring is strongly supported by the pushing forces (including buckling) which conform with the condition (a). However, in the currently explored parameter regime we do not observe stable spindle positioning near the septin ring when the cortical pull is acting alone (S7 Fig B) or in combination with the instantaneous push (Fig 6A, S7 Fig B, S7 Fig D-E). In special cases when (a) the average MT length is significantly large compared to the cell size, (b) there are many cMTs or (c) cMT segments keep sliding inside the cortex, the cortical pull may facilitate stable spindle positioning near the septin ring. Nevertheless, experiments indicate that the cMT number per SPB is limited and average MT length is of the order of the cell size in *C. neoformans* [14, 16] restricting the currently explored *in silico* parameter

regime.

It is important to mention that the analytical model is one-dimensional with simplified force expressions. Exploring the possibility of pulling mediated 'stable centering' in the current context is possibly beyond the scope of the analytical model presented here. Taking cues from other mechanistic models of MT aster positioning [85–88], a detailed mathematical model can be designed to further elucidate the mechanics of spindle positioning.

In summary, in the current study, we constructed a phenomenology based model that consistently explores various aspects of spindle assembly during mitotic cell division. Using the model, we have been able to elucidate several important features of MTOC clustering, nuclear migration, and spindle positioning, largely from a mechanistic point of view (Fig 7). While attempting to understand these processes in the light of dominant microtubule-based forces, (e.g. buckling or pulling from the cortex), we ignored weaker forces that may arise from sources *viz*, actin turnover, other molecular motors, thermal fluctuations, etc. Nevertheless, all these forces are important and a more realistic model should incorporate them in our future projects. Note that, the attributes of the dynamic processes involved in the mitotic cell cycle differ widely across different cell types. Different organisms evolved (with increasing complexity at the molecular level) to self-engineer the process of cell division. Thus, investigating the mechanistic principles of the cell division across different organisms using a systems biology-based approach in collaboration with molecular biology experiments stands as the subject of future research.

Materials and methods

Media and growth conditions

The wild-type and deletion mutant strains were grown in YPD (1 % yeast extract, 2 % peptone, 2 % dextrose) at 30° C. The conditional mutant strains were grown in YPG (1 % yeast extract, 2 % peptone, 2 % galactose) as a permissive medium and YPD as a non-permissive medium at 30° C. The strains used in this study are listed in S1 Table.

Microscopic image acquisition, live-cell imaging and processing

The wild-type and deletion mutant strains were grown in YPD overnight. The cells were washed with 1x phosphate-buffered saline (PBS) and the cell suspension was placed on agarose (2 %) patch present on the slide which was covered by a coverslip. The images were acquired at room temperature using laser scanning inverted confocal microscope LSM 880-Airyscan (ZEISS, Plan Apochromat 63x, NA oil 1.4) equipped with highly sensitive photo-detectors or Axio Observer Calibri (ZEISS). The Z-stack images were taken at every 0.5 μm and processed using ZEISS Zen software/ImageJ. Live-cell imaging was performed at 30°C on an inverted confocal microscope (ZEISS, LSM-880) equipped with a temperature-control chamber (Pecon incubator, XL multi SL), a Plan Apochromat 100x NA oil 1.4 objective and GaAsp photodetectors. Two-color images were taken by the sequential switching between RFP and GFP filter lines (GFP/FITC 488, mCherry 561 for excitation and GFP/FITC 500/550 band-pass, mCherry 565/650 long-pass for emission). For time-lapse microscopy of mCherry-CENP-A and GFP-Tub1, images were collected at a 2-min interval with 1.5 % intensity exposure and a 60-s interval with 1 % intensity exposure respectively, with 0.5 μm Z-steps. All the images were displayed after the maximum intensity projection of images at each time using ImageJ.

Post-acquisition analysis

The budding indices of cells were calculated as the ratio of the diameter of the daughter bud to the diameter of the mother bud. The diameters were measured by drawing a straight line using a line tool in ImageJ.

Simulation Procedure

Modeling the cellular confinement

The geometric construction of the whole cell is considered to be the intersection of two unequal spheres representing the mother bud (radius R_M) and the daughter bud (radius r_D). The septin ring is marked by the circle spanned at the intersection of the two spheres. The mother bud volume remains constant, while the growth rate of the daughter bud is tuned taking a cue from the experimental observations. The nucleus is taken as a sphere (radius r_{nuc}). Underneath the cell boundary, a cortical layer of finite width l_c accounts for the MT interaction at the cortex. The characteristic

Table 4. Description of MT based forces present in the *in silico* model

forces	origin	direction
instantaneous push ($F^{cell-mem}_{push-inst}$)	MT tip hitting the cell wall	directed along the MT, away from the cell wall
dynein mediated cortical pull (F^{cor}_{dyn})	MT sliding in cell cortex	directed along the MT, toward the cell cortex
Bim1 bias (F^{cor}_{Bim1})	cortical sliding of MTs toward septin ring	directed toward the septin ring
MT buckling (F^{cor}_{buckle})	MTs impinged on the cell boundary	directed along the MT, away from the cell cortex
inter cMT coupling	overlapping antiparallel MTs grazing the NE	directed along the MT, away from the cell cortex
push due to MT polymerization in cortex ($f^{MT-poly}_{cor}$)	cortical resistance on polymerizing MT tip	directed along the MT, away from the cell cortex
force at ipMT-ipMT overlap (f_{ipMT})	collective activity of kinesin-5 motors at ipMT-ipMT overlap	directed along the MT, leading to the separation of the SPBs
push by growing kMTs (f^{growth}_{push})	kMT tip penetrating into the KT	directed along the MT, away from the KT
pull by shrinking kMTs ($f^{shrinkage}_{pull}$)	separation between kMT tip and KT	directed along the MT, pulling the KT

parameters (e.g. dynein density etc.) of the cortical layer at the mother bud and the daughter bud are controlled independently due to possible functional differences at the molecular level [14, 16].

Modeling the MTs

MTs are modelled as semiflexible polymers characterized by four innate dynamic instability parameters, viz, growth velocity (v_g), shrinkage velocity (v_s), catastrophe frequency (f_c) and rescue frequency (f_r). While probing for an alternative mechanism, f_c of the MTs searching for the KT is modulated by the local concentration/gradient of the RanGTP like chemical. MTs hitting the cortex experience dynein pull, undergo buckling transition when pivoted and apply an instantaneous pushing force on the nucleus. A subpopulation of MTs, graze along the cortex and the NE.

Modeling MTOCs and kinetochores

The KTs and MTOCs are modeled similarly as done in the previous studies [14, 16]. MTOCs are rigid spheres on the outer NE and the movement of the MTOCs is strictly confined to the NE. The SPBs are considered as rigid spheres (radius r_{SPB}) embedded on the NE.

Spherical KTs with a hard-core repulsion ($\vec{f}_{intersection}$) prevent any finite overlap amongst the KTs. The repulsive force is proportional to the instantaneous overlap between two overlapping KTs [16]. Sister KTs remain paired with each other by the cohesin spring until metaphase. A Hookean force, proportional to the inter-KT separation, is introduced amongst the sister KTs to account for the effect of the cohesin spring holding them together [14, 16]. In the computational model, the Hookean force is given by $\vec{f}_{cohesin} = K_{cohesin}\vec{d}_{KT-KT}$, where $K_{cohesin}$ is the spring constant and $|\vec{d}_{KT-KT}|$ is the instantaneous separation between two sister KTs. Relevant model parameters are listed in Table 1. The description of various MT mediated force interactions is discussed in the following sections and summarized in Table 4.

Modeling cMT-cell cortex interaction and the inter cMT coupling at the NE

From the MTOCs and later from the SPBs, the cMTs nucleate in any random direction within the cell, excluding the nucleus. Various force transductions due to cMT-cell cortex interaction in the *in silico* model construction are categorically listed in the following.

1. When a growing cMT reaches to the cortex and hits the cell boundary, the steric cell boundary impedes the MT tip against its growth. We characterize the instantaneous force exerted on the MT tip upon each encounter with the cell boundary as an instantaneous push ($\vec{f}^{cell-mem}_{push-inst}$). The magnitude of the instantaneous push is taken to be 1 pN per MT on each encounter. The net instantaneous push is $\vec{F}^{cell-mem}_{push-inst}$= $\sum_{cMTs} \vec{f}^{cell-mem}_{push-inst}$.
2. Apart from the instantaneous push, a MT growing inside the cell cortex undergoes sliding. The 'bent' sliding segment inside the cell cortex provides anchorage points for the cortical dyneins. For computational simplicity, we introduce the parameter, mean number of dyneins per unit length in mother (daughter) cortex ($\lambda^{M(D)}_{dyn}$) on the MT segments inside the cortex. The force due to the dynein pull on a cMT ($\vec{f}^{cor}_{dyn}$) is proportional to $\lambda^{M(D)}_{dyn} l_{cor}$, where l_{cor} is the combined length of the penetrated MT segment inside the cell cortex. M, D in the suffix denotes mother and daughter bud cell cortex respectively. The net cortical dynein pull is $\vec{F}^{cor}_{dyn}$=$\sum_{cMTs} \vec{f}^{cor}_{dyn}$=$\sum_{cMTs} \lambda^{M(D)}_{dyn} l_{cor}\ \vec{f}_{dyn}$, where $\vec{f}_{dyn}$ is the force generated by a single dynein motor.
3. Similarly, the force due to Bim1 bias on a cMT within mother cortex is $\vec{F}^{cor}_{Bim1}$=$\sum_{cMTs} \vec{f}^{cor}_{Bim1}$=$\sum_{cMTs} \lambda^{M}_{Bim1} l_{cor}$ $\vec{f}_{Bim1}$ where $\vec{f}_{Bim1}$ is the force generated by a single Bim1 motor. The force due to Bim1 is directed toward the septin ring (Table 4). In the daughter cortex, there is no Bim1 bias. For simplicity, we chose λ^{M}_{Bim1}=λ^{M}_{dyn}.
4. The MTs impinged at the cell membrane also undergo buckling transition. MT buckling is a type of deformation of the MT under compressive loading force. Owing to the deformation, the MT imparts a restoring force which depends on the buckling length of the MT (estimated in [89]). We considered first-order Euler buckling in the present context. Whether a MT hitting the cell membrane, deep inside the cortex, will transduce dynein mediated pull or a net push away from the cortex due to Euler buckling or undergo catastrophe is dictated by predefined probabilities $P^{cell-mem}_{buckle}$, $P^{cell-mem}_{dyn-pull}$ and $P^{cell-mem}_{cat}$, where $P^{cell-mem}_{buckle}$ = 1- $P^{cell-mem}_{dyn-pull}$-$P^{cell-mem}_{cat}$. The buckling force ($\vec{f}^{cor}_{buckle}$) is proportional to l^{-2} where l is the concerned cMT length. The net buckling force is $\vec{F}^{cor}_{buckle}$= $\sum_{cMTs} \vec{f}^{cor}_{buckle}$ ($|\vec{f}^{cor}_{buckle}|$=$D_{buckle} l^{-2}$, where D_{buckle} refers to the flexural rigidity of the MT $\sim$ 200 pN μm^2) [55]. In mother cortex, $P^{cell-mem}_{dyn-pull}$=0.0, $P^{cell-mem}_{buckle}$=0.5, $P^{cell-mem}_{cat}$=0.5; in daughter cortex, $P^{cell-mem}_{dyn-pull}$=0.8, $P^{cell-mem}_{buckle}$=0.1, $P^{cell-mem}_{cat}$=0.1.
5. Moreover, a polymerizing MT at the cortex experiences resistance from the cortex on the MT tip in the vicinity of the cell membrane. The force exerted on the MT tip due to this resistance is chosen to be Hookean spring-like. We estimate the force on a polymerizing MT ($f^{MT-poly}_{cor}$) deep inside the cortex as $k_{cor} l_{cor}$. Here, k_{cor} is the equivalent spring constant characterizing $f^{MT-poly}_{cor}$ that pushes the MT tip away from the cortex. We evaluate the net push on the MTOCs/SPBs due to MT polymerization inside the cortex ($F^{MT-poly}_{cor}$) by summing the force contributions ($f^{MT-poly}_{cor}$) overall growing MTs within the cortical region ($F^{MT-poly}_{cor}$=$\sum^{cortex}_{MTs} f^{MT-poly}_{cor}$).

The overall load on a cMT at the cortex due to the resistance from the cortical substance modulates the dynamic instability parameters of the cMT. The intrinsic parameters v_g and f_c are tuned as described in the following: (a) $v_g = v_{g0} \exp(f_{load}/f_{stall})$, where v_{g0} represents the unimpeded growth velocity with no load exerted on the cMT, f_{load} and f_{stall} denote load force and stall force per cMT respectively; (b) f_c=f^{stall}_c/[1+ (f^{stall}_c/f_{c0} -1) exp (f_{load}/f_{stall})]. The load force $f_{load} \sim -k_{cor} l_{cor}$ [14,16].

To estimate the force due to the inter cMT coupling at the NE $\vec{f}_{overlap}$, we evaluate the net overlap length (l_{ovl}) between a pair of overlapping antiparallel MTs. The force exerted on the MTOCs is proportional to $\lambda_{ovl} l_{ovl}$, where λ_{ovl} is the mean number of minus end-directed motors per unit length at the MT-MT overlap on the NE.

Modeling nMT-kinetochore interaction

The nMTs are categorized into two distinct subsets, interdigitated MTs within the nuclear volume facilitating biorientation of SPBs via molecular motors i.e. interpolar MTs (ipMTs) and MTs establishing contact between SPBs and KTs i.e. kinetochore MTs (kMTs). The collective activity of crossbridging kinesin-5 motors at the ipMT-ipMT overlaps generates a force $f_{ipMT} = l^{ipMT}_{ovl} \lambda_{ipMT} f_{kinesin-5}$ where l^{ipMT}_{ovl} is the total overlapping length summed over all ipMTs emanating from two SPBs. λ_{ipMT} is the average number of kinesin-5 motors per unit length at the ipMT-ipMT overlap. $f_{kinesin-5}$ is the force exerted by a single kinesin-5 motor.

Stochastic growth and shrinkage of the kMTs due to dynamic instability leads to a tug of war between several

oppositely directed competing forces. During the growth phase of the kMT, the kMT tip imparts a net push $f_{push}^{growth} = l_{pen}K_{fibril}$ on the KT attached to it. Here, l_{pen} is the penetration length of the kMT into the KT, K_{fibril} is the stiffness constant of the connecting spring that mimics the KT fibril in the model. A kMT in shrinkage phase, pulls the KT with a force $f_{pull}^{shrinkage} = l_{separation}K_c$, where $l_{separation}$ is the distance between the kMT tip and the corresponding KT. K_c denotes the stiffness constant of the Hookean spring linking the depolymerizing kMT tip and the KT.

To maintain a constant gap between the SPBs and the KT cluster, a length-dependent catastrophe of the kMTs has been incorporated in the model. The catastrophe frequency of a kMT (f_c) is regulated in the following manner, $f_c = hl_{kMT}$, where l_{kMT} is the kMT length [14,16].

Equations of motions governing the spatiotemporal dynamics of the nucleus, MTOCs, kinetochores, SPBs

Forces due to single cMT interacting with the cortex, are applied on the nucleus and the MTOCs/SPBs, simultaneously. Additionally, the force stemming from the ipMT interaction is also exerted on the SPBs. If $\vec{F}_{nucleus}$, $\vec{F}_{MTOC}$ and $\vec{F}_{SPB}$ are the net resultant forces exerted on the nucleus, MTOC and SPB respectively, the corresponding equations of motion can be gleaned as,

$$\frac{d\vec{R}_{nucleus}}{dt} = \frac{\vec{F}_{nucleus}}{\zeta_{nucleus}} \tag{1}$$

$$\frac{d\vec{R}_{MTOC}}{dt} = \frac{\vec{F}_{MTOC}}{\zeta_{MTOC}} \tag{2}$$

$$\frac{d\vec{R}_{SPB}}{dt} = \frac{\vec{F}_{SPB}}{\zeta_{SPB}} \tag{3}$$

where $\vec{R}_{nucleus}$, $\vec{R}_{MTOC}$ and $\vec{R}_{SPB}$ denote the instantaneous positions of the nucleus, MTOCs and SPBs respectively, at a certain time step. $\zeta_{nucleus}$, ζ_{MTOC}, ζ_{SPB} represent viscous drag on the corresponding objects. $\vec{F}_{nucleus}$, $\vec{F}_{MTOC}$ and $\vec{F}_{SPB}$ contain vectorial contributions from $\vec{F}_{cor}^{MT-poly}$, $\vec{F}_{push-inst}^{cell-mem}$, $\vec{F}_{dyn}^{cor}$ and $\vec{F}_{buckle}^{cor}$. The net force on an MTOC $\vec{F}_{MTOC}$ is divided into two components: (a) tangential to the NE and (b) normal to the NE. As the movement of MTOC is considered constrained on NE, only the tangential force component is responsible for moving the MTOC on NE, the normal component is not allowed to contribute to the motion of MTOCs confined at the NE. The same procedure applies to the motion of the SPBs as well, as the SPBs are taken to be embedded on the NE throughout the mitotic period considered in the simulation. Due to the attachment of the MTOCs with the surface of the NE, the resultant force on the nucleus can be computed as the vectorial sum over the net cortical forces on individual MTOCs.

In a similar fashion, the motion of a KT is dictated by the following equation of motion,

$$\frac{d\vec{R}_{kinetochore}}{dt} = \frac{\vec{F}_{kinetochore}}{\zeta_{kinetochore}} \tag{4}$$

Here, $\vec{R}_{kinetochore}$, $\vec{F}_{kinetochore}$ and $\vec{\zeta}_{kinetochore}$ represent instantaneous position, net force on the KT and the viscous drag experienced by the KT respectively. $\vec{F}_{kinetochore}$ entails a vectorial summation over $\vec{f}_{push}^{growth}$, $\vec{f}_{pull}^{shrinkage}$, $\vec{f}_{ipMT}$, $\vec{f}_{cohesin}$ and $\vec{f}_{intersection}$. For simplicity, we have not considered contributions of thermal diffusion (Brownian motion) while computing the positional update of any of the objects considered in the model.

The equations of motion are discretized and solved using Euler's method at every time step.

Mathematical model for spindle positioning in budding yeast

In 2-dimensions we consider that the mother and the daughter bud constitute two intersecting circles of radii R_M and r_D respectively. The axis of symmetry of the cellular confinement (e.g. the mother-daughter conglomerate) is taken to be the X-axis with the origin 'O' at the center of the mother bud. The center of the daughter bud is placed at a distance 'd' from the center of the mother (Fig 3B-3C). We compute various MT-based forces on the spindle

upon MT interaction with the cell cortex. The mathematical formulation of various force balance terms (e.g. forces originating from MT pushing, dynein mediated pull on the MTs at the cell cortex, MT buckling, etc.) is characterized by exponential length distribution of MTs [36, 49, 55]. The direction of the forces is depicted in Fig 3C.

Pushing forces

MTs are nucleated from the two SPBs separated by a distance of $2a$ (spindle length) with spindle-center at x. For convenience, we mark the SPB located at the left of the spindle ($SPB(L)$) and the SPB located at the right of the spindle ($SPB(R)$). When an MT nucleates out of the $SPB(L)$, it grows a distance $R_M + x - a$ to establish contact with the cell membrane (3B). Hence, the instantaneous pushing force on the $SPB(L)$ due to the MTs hitting the mother bud cell membrane reads,

$$F_{push-inst}^{cell-mem(M)} = A_M e^{-(R_M+x-a)/L_{MT}^{av}} \tag{5}$$

The exponential weight factor enters the expression due to the length of dynamic MTs governed by the following distribution: $N(l) \propto e^{-l/L_{MT}^{av}}$ where l is the length of the MT under consideration. The instantaneous pushing force from the MTs nucleating out of the $SPB(R)$ has to elongate up to a distance $d + r_D - x - a$ along the axis of symmetry to make a contact with the cell membrane in the daughter bud. Hence, the instantaneous pushing force contribution from the daughter bud cell membrane is,

$$F_{push-inst}^{cell-mem(D)} = -A_D e^{-(d+r_D-x-a)/L_{MT}^{av}} \tag{6}$$

Here A_M and A_D define the amplitude of the instantaneous pushing force contribution from the mother and the daughter bud cell membrane. The prefactors A_M and A_D are proportional to the number of MTs interacting with the cell membrane where instantaneous pushing force per MT is taken to be ~ 1 pN.

Pulling forces

When an MT emanating from the $SPB(L)$ grows all the way to penetrate the mother cortex, the dyneins localized at the cortex anchor to the MT segment orchestrating a net pull ($F_{dyn}^{cor(M)}$) toward the mother cortex. Since an elongating MT segment inside the cortex can bend and undergoes sliding as illustrated in the schematic diagram, the pulling force is categorized into two parts: 1. the pull on the uncurled/straight MT segment in the cortex and 2. the pull on the MT segment engaged in 'lateral sliding' along the cortex. Similarly, MTs nucleating out of the $SPB(R)$ upon elongating up to the daughter cortex can penetrate and experience dynein mediated pull. For an MT nucleating from the $SPB(L)$ within the one-dimensional confinement, it has to extend at least up to a distance of $R_M - l_c + x - a$ to establish physical contact with the mother cortex. It is also evident from the schematic diagram that after reaching the cortex the 'uncurled' MT tip can advance up to $R_M + x - a$ without bending (Fig 3B). Henceforth the net pull on the $SPB(L)$ from the 'uncurled' MT segments in the mother cortex can be evaluated in the following manner.

$$\begin{aligned} F_{dyn(uncurled)}^{cor(M)} &= -B_M \lambda_{dyn}^M \int_{R_M-l_c+x-a}^{R_M+x-a} e^{-s/L_{MT}^{av}} ds \\ &= -B_M \lambda_{dyn}^M L_{MT}^{av} (e^{l_c/L_{MT}^{av}} - 1) e^{-(R_M+x-a)/L_{MT}^{av}} \end{aligned} \tag{7}$$

In a similar manner, we can also evaluate the net dynein pull contribution from the 'arc' like MT segment sliding within the mother cortex. Therefore, the net force due to the dynein pull on the sliding 'arc' $F_{dyn(sliding)}^{cor(M)}$ reads

$$\begin{aligned} F_{dyn(sliding)}^{cor(M)} &= -B_M \lambda_{dyn}^M \int_0^{l_{arc}^M} ds\ e^{-(R_M+x-a+s)/L_{MT}^{av}} \\ &= -B_M \lambda_{dyn}^M L_{MT}^{av} e^{-(R_M+x-a)/L_{MT}^{av}} (1 - e^{-l_{arc}^M/L_{MT}^{av}}) \end{aligned} \tag{8}$$

Here l_{arc}^M is the 'arc' like segment traced from the intersection of the axis of symmetry and the mother bud cell membrane to the peripheral contact of the septin ring with the mother bud cell membrane. Here for the sake of simplicity, we assume that the sliding MTs passing through the mother cortex extend up to the septin ring. The value of l_{arc}^M is estimated to be

$$l_{arc}^M = \frac{\pi R_M}{2} + R_M \tan^{-1}(x_{sp}/y_{sp}) \tag{9}$$

From $SPB(R)$ we assume that the MTs nucleate in the direction of the daughter bud and interact with the daughter cortex and orchestrate a pull ($F_{dyn}^{cor(D)}$) in a similar fashion with which MTs from $SPB(L)$ interact with the mother cortex. Thus, the net pull due to the anchored dyneins on the 'uncurled' MT segments inside the daughter cortex reads,

$$\begin{aligned} F_{dyn(uncurled)}^{cor(D)} &= B_D \lambda_{dyn}^D \int_{d+r_D-l_c-(x+a)}^{d+r_D-(x+a)} ds\ e^{-s/L_{MT}^{av}} \\ &= B_D \lambda_{dyn}^D L_{MT}^{av} (e^{l_c/L_{MT}^{av}} - 1) e^{-(d-x-a+r_D)/L_{MT}^{av}} \end{aligned} \tag{10}$$

Similarly, we can compute the contribution in the net dynein pull on $SPB(R)$ from the 'sliding arc' passing through the daughter cortex in the following manner.

$$\begin{aligned} F_{dyn(sliding)}^{cor(D)} &= B_D \lambda_{dyn}^D \int_0^{l_{arc}^D} ds\ e^{-(d+r_D-x-a+s)/L_{MT}^{av}} \\ &= B_D \lambda_{dyn}^D L_{MT}^{av} e^{-(d+r_D-x-a)/L_{MT}^{av}} (1 - e^{-l_{arc}^D/L_{MT}^{av}}) \end{aligned} \tag{11}$$

Here, l_{arc}^D is estimated to be the arc length traced from the intersection of the axis of symmetry with the daughter cortex and the peripheral contact of the septin ring with the cell membrane. From the schematic diagram we obtain the l_{arc}^D to be

$$l_{arc}^D = \frac{\pi r_D}{2} + r_D \tan^{-1}\left(\frac{d - x_{sp}}{y_{sp}}\right) \tag{12}$$

Note here that the prefactors B_M and B_D are proportional to the number of MTs experiencing dynein mediated pulling in the mother and the daughter cortex respectively.

In the above analysis, we have assumed that the effective dynein density is smeared uniformly across the whole mother and daughter cortex. However, experimental observations point toward a non-uniform, differential spatial arrangement of dyneins in the mother and the daughter cortex. These observations prompted us to accommodate the differential spatial profiling of dynein in the mother and the daughter cortex into the current mathematical model. Force transduction due to the differential spatial organization of dyneins in the mother and daughter cortex is described in detail in the S1 Text.

Buckling forces

MTs with tips passed into the mother(daughter) cortex can buckle where the buckling probability is a tunable parameter in the current model. MTs impinged and pivoting at the mother(daughter) cortex generate a length-dependent 'pushing' force that increases with the squared inverse length of the MT while undergoing buckling. It is evident from the geometric construction that the forces stemming from MT buckling at the mother and daughter cortex are oppositely directed (Fig 3C). We have taken the following form for the force produced by cortical buckling at the mother cortex ($F_{buckle}^{cor(M)}$)

$$F_{buckle}^{cor(M)} = \frac{D_M}{(R_M + x - a)^2}\ e^{-(R_M+x-a)/L_{MT}^{av}} \tag{13}$$

Similarly, force generated due to the buckling at the daughter cortex $F_{buckle}^{cor(D)}$ is taken as

$$F_{buckle}^{cor(D)} = -\frac{D_D}{(d + r_D - x - a)^2}\ e^{-(d+r_D-x-a)/L_{MT}^{av}} \tag{14}$$

D_M and D_D are proportional to the buckling amplitude times the average number of MTs undergoing buckling transition in the mother and daughter cortices, respectively.

Supporting Information

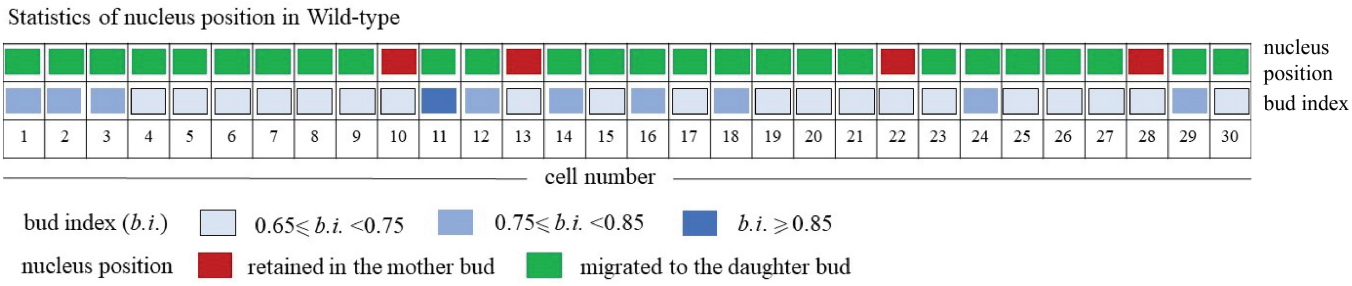

S1 Fig. Statistics of whether the nucleus is localized in mother bud or daughter bud in wild-type cells. Each column represents a cell indicating the color-coded status of its bud index and the localization of the nucleus within the cell.

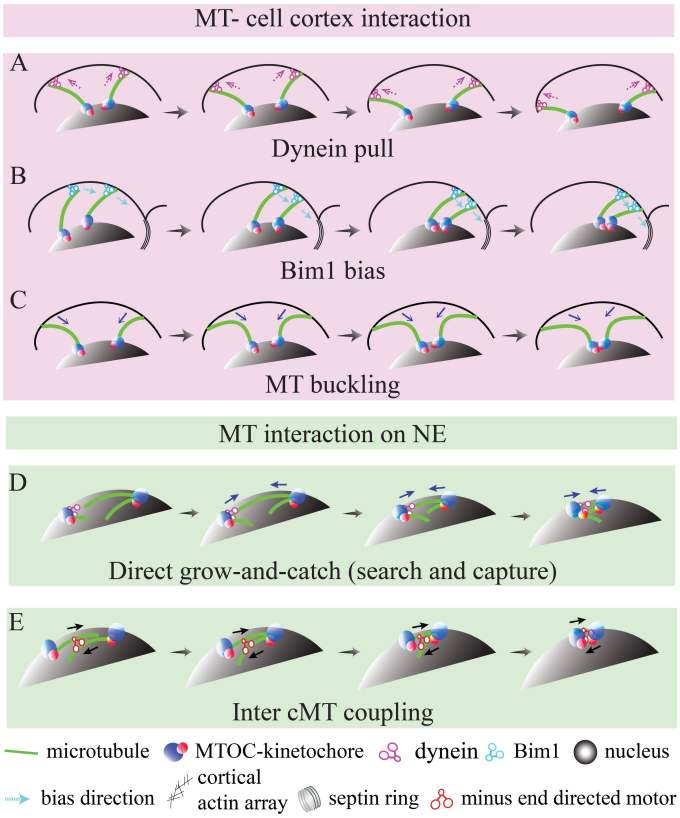

S2 Fig. Schematic depicting the movement of MTOCs under the effect of various MT mediated forces accounted in the model. (A-C) Representative cartoons illustrate the trajectory of MTOCs due to various forces originating from MT-cell cortex interaction: dynein pull (A), Bim1 bias (B), MT buckling (C). (D-E) Representative cartoons illustrate the trajectory of MTOCs due to various forces originating from MT interaction on NE: MTs directly 'grow-and-catch' MTOCs (D) and inter cMT coupling on NE via minus end-directed motors (E).

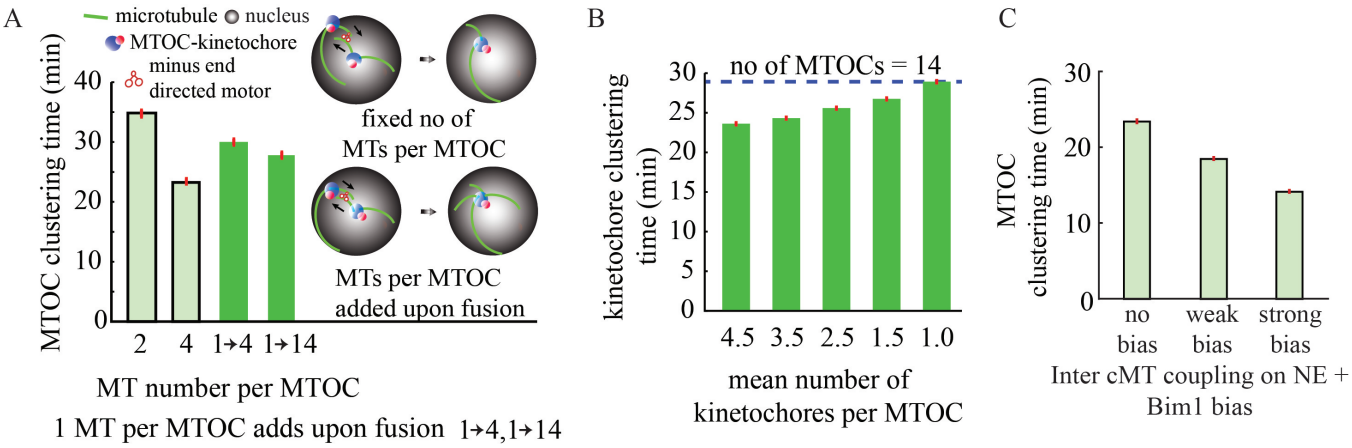

S3 Fig. Additional numerical tests for MTOC clustering. (A) (First and second bars from left) MTOC clustering time with a fixed number of cMTs per MTOC. Clustering solely via 'inter cMT coupling at the NE' is considered here. (Third bar, $1 \rightarrow 4$) Clustering time when every MTOC nucleates a single cMT initially and upon the fusion of the MTOCs the MTs aggregate up to a maximum of 4 cMTs per MTOC. (Fourth bar, $1 \rightarrow 14$) Similar to the "Third bar" but no constraint on the number of cMTs that can add up to the number of MTOCs. (B) Asynchronous assembly of KTs/MTOCs, if more than one KT is associated with a single MTOC. (C) MTOC clustering time when two proposed modes of MTOC clustering namely 1. the inter cMT coupling on NE and 2. MT-cell cortex interaction having enhanced Bim1 bias and diminished cortical pull are considered to be acting together.

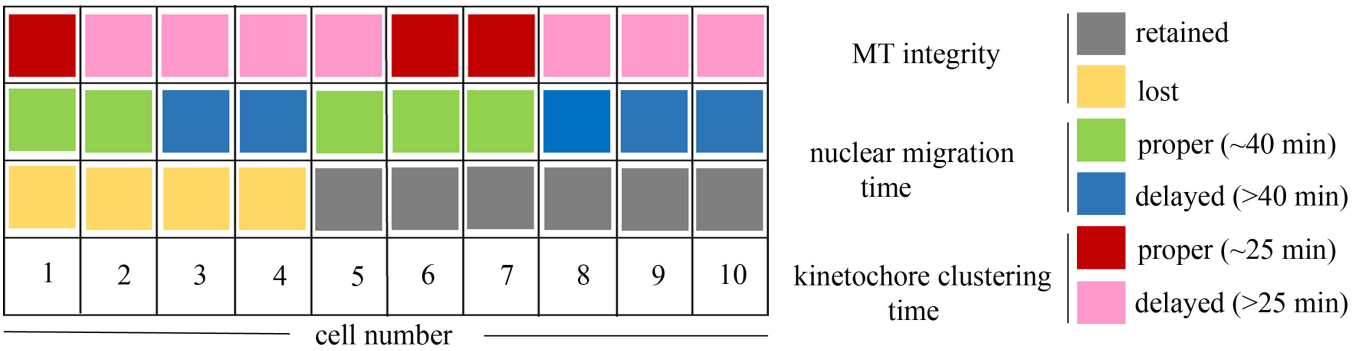

S4 Fig. Distribution of cells showing variations in MT integrity, nuclear migration duration and KT clustering timing upon Ipl1-depletion. Each column represents a cell indicating the color-coded status of the MT integrity, the time required for nuclear migration and KT clustering. Note that the Ipl1 depletion is facilitated by employing the well-characterized GAL7 promoter system throughout many cell cycles in an unsynchronized cell colony. This is likely to be a plausible reason behind the observed heterogeneity among phenotypes of impaired KT clustering, nuclear migration and MT integrity.

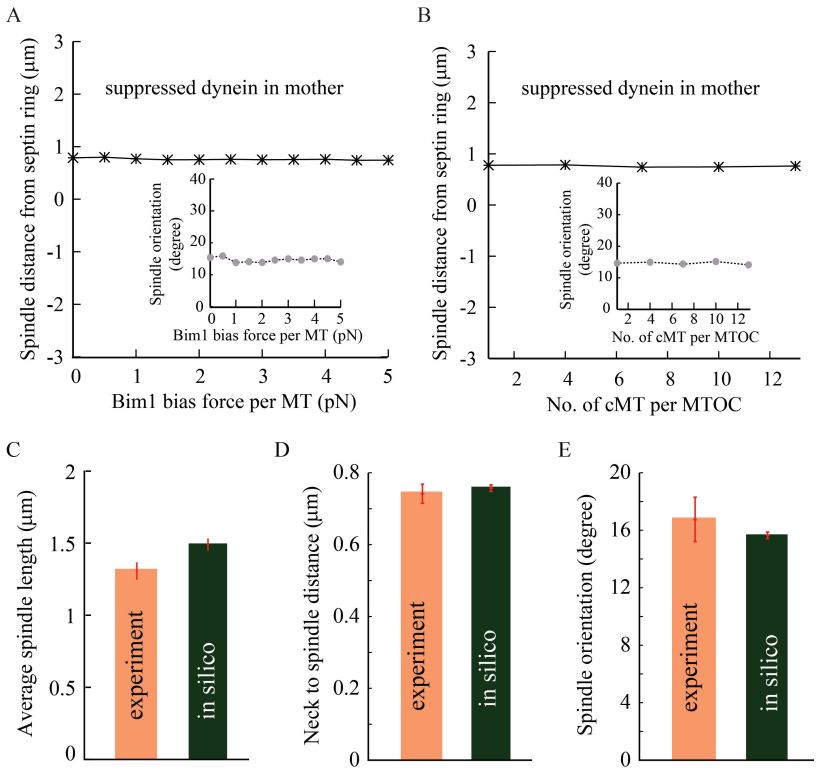

S5 Fig. Multiple characteristics of spindle architecture and localization. (A-B) Spindle distance from septin ring and spindle orientation (inset) relative to the axis joining the center of the mother and daughter bud when the magnitude of force per MT due to Bim1 bias (A) and the number of cMT per MTOC (B) are varied. The spindle position and orientation turn out to be insensitive to the variations in Bim1 bias force per MT and the number of cMT per MTOC in the explored parameter regime. (C) The length of the spindle (n=68, experiment) in metaphase cells is shown. (D) The spindle to neck (junction of mother-daughter bud) distance in the wild-type (n=70, experiment). (E) The spindle orientation with respect to the mother-daughter axis (n=52, experiment). The +ve/-ve sign in distance indicates the spindle position inside the daughter/mother bud. In all figures, n > 2000 for simulation and red bars indicate SEM (wherever shown).

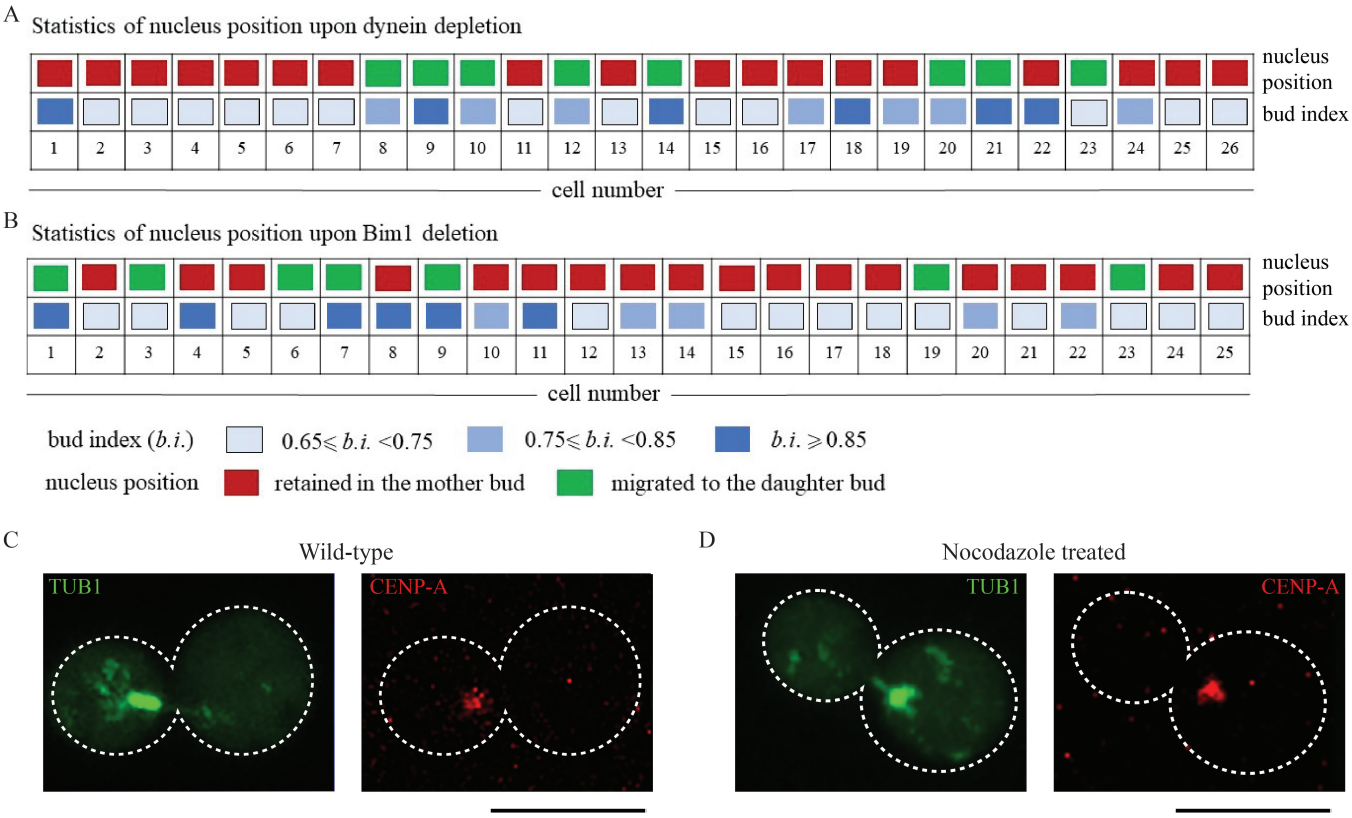

S6 Fig. Nucleus position within cells upon various molecular perturbations. (A-B) Each column represents a cell indicating the color-coded status of its bud index and the localization of the nucleus within the cell. The statistics/distribution shows the nucleus position (whether the nucleus is localized in the mother bud or the daughter bud) upon dynein depletion (A), Bim1 deletion (B). (C-D) Images of cells showing localization of MTs (GFP-TUB1) and KTs (mCherry-CENP-A) in large budded wild-type (C) and nocodazole treated cells (D). Bar, 5 μm.

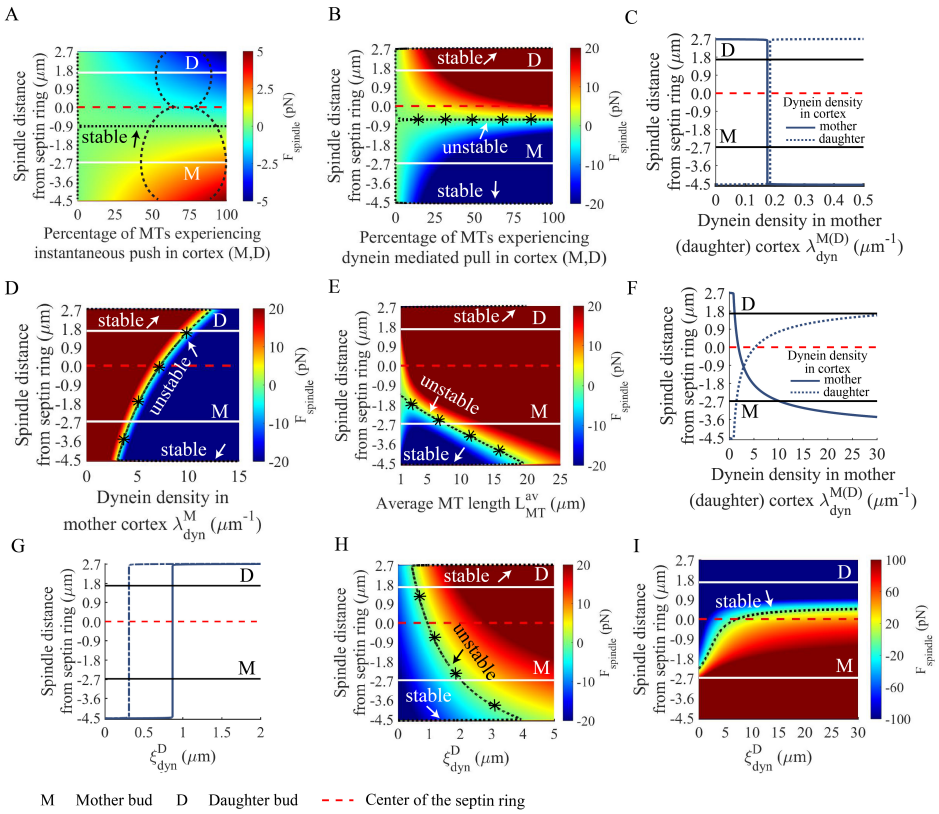

S7 Fig. Effect of various force combinations on spindle positioning. In all figures, -ve/+ve distance refers to the spindle in mother (M)/daughter (D) bud. In the color maps, white solid lines denote the center of the daughter and mother bud; color bars represent net force on the spindle. (A) In presence of instantaneous cortical push from the mother and daughter cortex, the spindle stabilizes (dotted black line) close to the septin ring inside the mother bud. (B) In presence of dynein mediated cortical pull from the mother and daughter cortex, the spindle collapses onto the cell cortex. An unstable spindle position is found in between. (C) Variation in dynein pull from mother (daughter) cortex ($\lambda_{dyn}^{M(D)}$) with instantaneous cortical push from mother (daughter) cortex acting alongside. The spindle collapses either onto the mother cortex or onto the daughter cortex. Forces are exerted solely from mother (daughter) cortex. (D) Spindle position upon variation in dynein density in the mother cortex (λ_{dyn}^{M}) with fixed dynein density in the daughter cortex. Instantaneous cortical push is present in both mother and daughter. (E) Spindle position upon variation in average MT length (L_{MT}^{av}) when instantaneous cortical push and dynein pull are combined. (F) Spindle position upon variation in dynein density in mother (daughter) cortex ($\lambda_{dyn}^{M(D)}$) when instantaneous push, dynein pull, and MT buckling in mother (daughter) cortex act together. MT buckling force (directed away from cortex) dominates close to the mother (daughter) cortex. Forces are exerted solely from mother (daughter) cortex. (G) Variation of the characteristic length scale spanning the localized dynein patch in the daughter cortex (ξ_{dyn}^{D}) yields unstable spindle positions slotted in between stable fixed positions of the spindle position in the mother and the daughter cortex while mutually opposing MT mediated instantaneous push and dynein pull solely from the daughter cortex compete against each other. For this particular scenario, force transduction from the mother cortex is switched 'off'. Relevant parameters: $\lambda_{dyn}^{D} = 1\ \mu\text{m}^{-1}$ (solid line) and $2\ \mu\text{m}^{-1}$ (dashed line), $A_D = 5$ pN. (H) Variation in the characteristic length scale accounting for the size of localized dynein patches in the daughter cortex (ξ_{dyn}^{D}) results in unstable fixed positions as the spindle undergoes a gradual spatial transition from the stable fixed positions at the mother cortex to the stable fixed positions at the daughter cortex. The force balance landscape is governed by cortical pull stemming from the mother and daughter cortex only (relevant parameters: λ_{dyn}^{M} =1 μm^{-1}; $\lambda_{dyn}^{D} = 4.5\ \mu\text{m}^{-1}$). (I) In presence of MT buckling transition together with instantaneous push and dynein pull from the mother and the daughter cortex, stepwise increment in ξ_{dyn}^{D} enhances net pull toward the daughter resulting in a stable spindle positioning inside the daughter bud.

S1 Text. Mechanisms of MTOC clustering and spindle positioning in the budding yeast *Cryptococcus neoformans*: a microtubule grow-and-catch model. This file comprises the following sections: 1. *One-dimensional mathematical model describing the forces due to localized dynein organization in the daughter bud cell cortex.* This section describes the mathematical calculation of estimating cortical pull when the spatial organization of dyneins is localized. 2. *Analytical model assumptions and comparisons with the agent-based model.* This section discusses the assumptions considered in the analytical model of spindle positioning and compares the analytical model with the agent-based model. 3. *Additional numerical analysis of MTOC clustering (agent-based model).* This section provides details about the additional numerical tests carried out to explore the dependence of MTOC clustering on various model parameters. 4. *Additional numerical analysis of spindle positioning (analytical model).* This section explores the combinatory effects of various MT mediated forces on proper spindle positioning. (PDF)

S1 Video. Cell cycle stages in *C. neoformans* wild-type cell. Wild-type cells expressing GFP-Tub1 were imaged after every 2 min by confocal microscopy. KTs (CENP-A) were visualized by mCherry-tagged CENP-A. The video corresponds to the still images from Fig 1.

S2 Video. MTOC clustering facilitated via inter-cMT coupling at the nuclear envelope (NE). MTOCs are blue; KTs are magenta; MTs are green.

S3 Video. MTOC clustering facilitated via MT-cell cortex interaction. Force produced by single dynein on each MT at mother cortex ($|\vec{f}_{dyn}|$) is chosen to be 1.0 pN. Bias force towards septin ring produced by single Bim1 on each MT at mother cortex ($|\vec{f}_{Bim1}|$) is chosen to be 0.0 pN. MTOCs are blue; KTs are magenta; MTs are green.

S4 Video. MTOC clustering facilitated via MT-cell cortex interaction (enhanced Bim1 bias + suppressed dynein activity). Force produced by single dynein on each MT at mother cortex ($|\vec{f}_{dyn}|$) is chosen to be 0.0 pN. Bias force towards septin ring produced by single Bim1 on each MT at mother cortex ($|\vec{f}_{Bim1}|$) is chosen to be 1.0 pN. MTOCs are blue; KTs are magenta; MTs are green.

S1 Table. List of strains used in this study (DOCX)

Acknowledgments

This work was supported by the fellowship from SERB (Science and Engineering Research Board), Department of Science and Technology (DST), India (EMR/2017/001346) to RP and Tata Innovation Fellowship (BT/HRD/35/01/03/2017) to KS. SC was supported by fellowship from the University Grants Commission (UGC), India, SS was supported by the fellowship from INSPIRE (IF131156) program DST, India, and NV was supported by the fellowships (09/733 (0253)/219-EMR-I) and 9/733 (0161)/2011-EMR-I from Council of Scientific & Industrial Research (CSIR), India.

References

1. Dogterom M, Leibler S. Physical Aspects of the Growth and Regulation of Microtubule Structures. Physical Review Letters. 1993;70(9):1347–1350.
2. Wu J, Akhmanova A. Microtubule-Organizing Centers. Annu Rev Cell Dev Biol. 2017;33:4.1–4.25.
3. Bornens M. The centrosome in cells and organisms. Science. 2012;335:422–26.
4. Conduit PT, Wainman A, Raff JW. Centrosome function and assembly in animal cells. Nat Rev Mol Cell Biol. 2015;16:611–24.
5. Rodionov V, Nadezhdina E, Borisy G. Centrosomal control of microtubule dynamics. PNAS. 1999;96:115–20.
6. Chabin-Brion K, Marceiller J, Perez F, Settegrana C, Drechou A, Durand G, et al. The Golgi complex is a microtubule-organizing organelle. Mol Biol Cell. 2001;12:2047–60.

7. Hurtado L, Caballero C, Gavilan MP, Cardenas J, Bornens M, Rios RM. Disconnecting the Golgi ribbon from the centrosome prevents directional cell migration and ciliogenesis. Journal of Cell Biology. 2011;193:917–33.

8. Vinogradova T, Paul R, Grimaldi AD, Loncarek J, Miller PM, Yampolsky D, et al. Concerted effort of centrosomal and Golgi-derived microtubules is required for proper Golgi complex assembly but not for maintenance. Mol Biol Cell. 2012;23:820–33.

9. Vinogradova T, Miller PM, Kaverina I. Microtubule network asymmetry in motile cells: role of Golgi-derived array. Cell Cycle. 2009;8:2168–74.

10. Paz J, Lüders J. Microtubule-Organizing Centers: Towards a Minimal Parts List. Trends in Cell Biology. 2018;28(3):176–187.

11. Kilmartin JV. Lessons from yeast: the spindle pole body and the centrosome. Philos Trans R Soc Lond B Biol Sci. 2014;369:20130456.

12. chen Lin T, Neuner A, Schiebel E. Targeting of gamma-tubulin complexes to microtubule organizing centers: conservation and divergence. Trends Cell Biol. 2014;25:296–307.

13. chen Lin T, Neuner A, Schlosser YT, Scharf AN, Weber L, Schiebel E. Cell-cycle dependent phosphorylation of yeast pericentrin regulates γ-TuSC-mediated microtubule nucleation. Elife. 2014;3:e02208.

14. Sutradhar S, Yadav V, Sridhar S, Sreekumar L, Bhattacharyya D, Ghosh SK, et al. A comprehensive model to predict mitotic division in budding yeasts. Molecular Biology of the Cell. 2015;26(22):3954–3965.

15. Kozubowski L, Yadav V, Chatterjee G, Sridhar S, Yamaguchi M, Kawamoto S, et al. Ordered Kinetochore Assembly in the Human-Pathogenic Basidiomycetous Yeast Cryptococcus neoformans. mBio. 2013;4(5):00614–13.

16. Varshney N, Som S, Chatterjee S, Sridhar S, Bhattacharyya D, Paul R, et al. Spatio-temporal regulation of nuclear division by Aurora B kinase Ipl1 in Cryptococcus neoformans. PLoS Genet. 2019;15(2):e1007959.

17. Heitman J. Microbial Pathogens in the Fungal Kingdom. Fungal Biol Rev. 2011;25(1):48–60.

18. Janbon G, Ormerod KL, Paulet D, 3rd EJB, Yadav V, Chatterjee G, et al. Analysis of the genome and transcriptome of Cryptococcus neoformans var. grubii reveals complex RNA expression and microevolution leading to virulence attenuation. PLoS Genet. 2014;10:e1004261.

19. Srikanta D, Santiago-Tirado F, Doering T. Cryptococcus neoformans: historical curiosity to modern pathogen. Yeast. 2014;31(2):47–60.

20. Varshney N, Sanyal K. Nuclear migration in budding yeasts: position before division. Current Genetics. 2019;65:1341–1346.

21. Rasmussen CG, Humphries JA, Smith LG. Determination of Symmetric and Asymmetric Division Planes in Plant Cells. Annual Review of Plant Biology. 2011;62:387–409.

22. Byers B, Goetsch L. Behavior of spindles and spindle plaques in the cell cycle and conjugation of Sacscharomyces cerevisiae. J Bacteriol. 1975;124(1):511–23.

23. Winey M, O'Toole E. The spindle cycle in budding yeast. Nat Cell Biol. 2001;3(1):E23–7.

24. Souza CD, Osmani S. Mitosis, Not Just Open or Closed. Eukaryot Cell. 2007;6(9):1521–27.

25. Yadav V, Sanyal K. Sad1 Spatiotemporally Regulates Kinetochore Clustering To Ensure High-Fidelity Chromosome Segregation in the Human Fungal Pathogen Cryptococcus neoformans. mSphere. 2018;3(4):e00190–18.

26. Yamaguchi M, Biswas SK, Kuwabara Y, Ohkusu M, Shimizu M, Takeo K. The spindle pole body of the pathogenic yeast *Cryptococcus neoformans*: variation in morphology and positional relationship with the nucleolus and the bud in interphase cells. Journal of Electron Microscopy. 2010;59(2):165–172.

27. Yamaguchi M, Ohkusu M, Biswas S, Kawamoto S. Cytological study of cell cycle of the pathogenic yeast Cryptococcus neoformans. Nihon Ishinkin Gakkai Zasshi. 2007;48(4):147–52.

28. Tanaka T, Stark M, Tanaka K. Kinetochore capture and bi-orientation on the mitotic spindle. Nat Rev Mol Cell Biol. 2005;6(12):929–42.

29. Thakur J, Sanyal K. The essentiality of the fungus-specific Dam1 complex is correlated with a one-kinetochore-one-microtubule interaction present throughout the cell cycle, independent of the nature of a centromere. Eukaryot Cell. 2011;10:1295–305.

30. Thakur J, Sanyal K. A coordinated interdependent protein circuitry stabilizes the kinetochore ensemble to protect CENP-A in the human pathogenic yeast Candida albicans. PLoS Genet. 2012;8:e1002661.

31. Gladfelter A, Berman J. Dancing genomes: fungal nuclear positioning. Int Rev Cytol. 2009;7(12):875–86.

32. Heath IB. Variant mitoses in lower eukaryotes: indicators of the evolution of mitosis. Int Rev Cytol. 1980;64:1–80.

33. Straube A, Brill M, Oakley B, Horio T, Steinberg G. Microtubule organization requires cell cycle-dependent nucleation at dispersed cytoplasmic sites: polar and perinuclear microtubule organizing centers in the plant pathogen *Ustilago maydis*. Mol Biol Cell. 2003;14:642–657.

34. Piel M, Tran PT. Cell Shape and Cell Division in Fission Yeast. Current Biology. 2009;19 (17):R823–R827.

35. Sawin KE, Lourenco PCC, Snaith HA. Microtubule Nucleation at Non-Spindle Pole Body Microtubule-Organizing Centers Requires Fission Yeast Centrosomin-Related Protein mod20p. Current Biology. 2004;14:763–775.

36. Chatterjee S, Sarkar A, Zhu J, Khodjakov A, Mogilner A, Paul R. Mechanics of multi-centrosomal clustering in bipolar mitotic spindles. Biophysical Journal. 2020;119(2):434–447.

37. Kiyomitsu T, Cheeseman IM. Chromosome- and spindle- pole-derived signals generate an intrinsic code for spindle position and orientation. Nat Cell Biol. 2012;14:311–317.

38. Park DH, Rose LS. Dynamic localization of LIN-5 and GPR-1/2 to cortical force generation domains during spindle positioning. Dev Biol. 2008;315:42–54.

39. McNally FJ. Mechanisms of spindle positioning. J Cell Biol. 2013;200(2):131–140.

40. Théry M, Jiménez-Dalmaroni A, Racine V, Bornens M, Julicher F. Experimental and theoretical study of mitotic spindle orientation. Nature. 2007;447(7143):493–6.

41. Minc N, Burgess D, Chang F. Influence of cell geometry on division-plane positioning. Cell. 2011;144(3):414–26. doi:10.1016/j.cell.2011.01.016.

42. Gay G, Courtheoux T, Reyes C, Tournier S, Gachet Y. A stochastic model of kinetochore-microtubule attachment accurately describes fission yeast chromosome segregation. J Cell Biol. 2012;196(6):757–74. doi:10.1083/jcb.201107124.

43. Pavin N, Tolic IM. Self-Organization and Forces in the Mitotic Spindle. Annu Rev Biophys. 2016;45:279–98. doi:10.1146/annurev-biophys-062215-010934.

44. Zaytsev AV, Segura-Pena D, Godzi M, Calderon A, Ballister ER, Stamatov R, et al. Bistability of a coupled Aurora B kinase-phosphatase system in cell division. Elife. 2016;5:e10644. doi:10.7554/eLife.10644.

45. Elting MW, Prakash M, Udy DB, Dumont S. Mapping Load-Bearing in the Mammalian Spindle Reveals Local Kinetochore Fiber Anchorage that Provides Mechanical Isolation and Redundancy. Curr Biol. 2017;27(14):2112–2122.e5. doi:10.1016/j.cub.2017.06.018.

46. Li J, Cheng L, Jiang H. Cell shape and intercellular adhesion regulate mitotic spindle orientation. Mol Biol Cell. 2019;30(19):2458–2468. doi:10.1091/mbc.E19-04-0227.

47. Letort G, Bennabia I, Dmitrieffb S, Nedelec F, Verlhaca MH, Terreta ME. A computational model of the early stages of acentriolar meiotic spindle assembly. Mol Biol Cell. 2019;30(7):863–875.

48. Lamson AR, Edelmaier CJ, Glaser MA, Betterton MD. Theory of Cytoskeletal Reorganization during Cross-Linker-Mediated Mitotic Spindle Assembly. Biophysical Journal. 2019;116:1719–1731.

49. Ferenz NP, Paul R, Fagerstrom C, Mogilner A, Wadsworth P. Dynein antagonizes Eg5 by crosslinking and sliding antiparallel microtubules. Curr Biol. 2009;19(21):1833–1838.

50. Nedelec F. Computer simulations reveal motor properties generating stable antiparallel microtubule interactions. J Cell Biol. 2002;158(6):1005–15.

51. Wollman R, Civelekoglu-Scholey G, Scholey JM, Mogilner A. Reverse engineering of force integration during mitosis in the Drosophila embryo. Mol Syst Biol. 2008;4:195.

52. Rubinstein B, Larripa K, Sommi P, Mogilner A. The elasticity of motor-microtubule bundles and shape of the mitotic spindle. Phys Biol. 2009;6(1):016005.

53. Kalinina I, Nandi A, Delivani P, Chacón MR, Klemm AH, Ramunno-Johnson D, et al. Pivoting of microtubules around the spindle pole accelerates kinetochore capture. Nat Cell Biol. 2013;15(1):82–87.

54. Maiato H, Gomes AM, Sousa F, Barisic M. Mechanisms of Chromosome Congression during Mitosis. Biology (Basel). 2017;6(1). doi:10.3390/biology6010013.

55. Som S, Chatterjee S, Paul R. Mechanistic three-dimensional model to study centrosome positioning in the interphase cell. Phys Rev E. 2019;99:012409.

56. Korinek WS, Copeland MJ, Chaudhuri A, Chant J. Molecular linkage underlying microtubule orientation toward cortical sites in yeast. Science. 2000;287:2257–2259.

57. Lee L, Tirnauer JS, Li J, Schuyler SC, Liu JY, Pellman D. Positioning of the mitotic spindle by a cortical-microtubule capture mechanism. Science. 2000;287:2260–2262.

58. Miller RK, Cheng SC, Rose MD. Bim1p/Yeb1p mediates the Kar9p-dependent cortical attachment of cytoplasmic microtubules. Mol Biol Cell. 2000;11:2949–2959.

59. Cepeda-García C, Delgehyr N, Ortiz MAJ, ten Hoopen R, Zhiteneva A, Segal M. Actin-mediated Delivery of Astral Microtubules Instructs Kar9p Asymmetric Loading to the Bud-Ward Spindle Pole. Molecular Biology of the Cell. 2010;21(15):2685–2695.

60. Shulist K, Yen E, Kaitna S, Leary A, Decterov A, Gupta D, et al. Interrogation of γ-tubulin alleles using high-resolution fitness measurements reveals a distinct cytoplasmic function in spindle alignment. Scientific Reports. 2017;7:11398.

61. Lee SC, Heitman J. Function of Cryptococcus neoformans KAR7 (SEC66) in karyogamy during unisexual and opposite-sex mating. Eukaryot Cell. 2012;11(6):783–94.

62. Lee IJ, Wang N, Hu W, Schott K, Bahler J, Jr THG, et al. Regulation of spindle pole body assembly and cytokinesis by the centrin-binding protein Sfi1 in fission yeast. Mol Biol Cell. 2014;25(18):2735–2749.

63. Seybold C, Schiebel E. Spindle pole bodies. Current Biology. 2013;23(19):R858–R860.

64. Civelekoglu-Scholey G, Sharp DJ, Mogilner A, Scholey JM. Model of Chromosome Motility in Drosophila Embryos: Adaptation of a General Mechanism for Rapid Mitosis. Biophysical Journal. 2006;19(11):3966–3982.

65. Fink G, Schuchardt I, Colombelli J, Stelzer E, Steinberg G. Dynein-mediated pulling forces drive rapid mitotic spindle elongation in Ustilago maydis. EMBO J. 2006;25(20):4897–908.

66. Finley KR, Bouchonville KJ, Quick A, Berman J. Dynein-dependent nuclear dynamics affect morphogenesis in Candida albicans by means of the Bub2p spindle checkpoint. J Cell Sci. 2008;121:466–76.

67. Letort G, Nedelec F, Blanchoin L, Thery M. Centrosome centering and decentering by microtubule network rearrangement. Mol Biol Cell. 2016;27(18):2833–43.

68. Dogterom M, Yurke B. Measurement of the force-velocity relation for growing microtubules. Science. 1997;278(5339):856–60.

69. Soppina V, Rai AK, Ramaiya AJ, Barak P, Mallik R. Tug-of-war between dissimilar teams of microtubule motors regulates transport and fission of endosomes. Proc Natl Acad Sci USA. 2009;106(46):19381–6.

70. Muller MJI, Klumpp S, Lipowsky R. Tug-of-war as a cooperative mechanism for bidirectional cargo transport by molecular motors. Proc Natl Acad Sci USA. 2008;105(12):4609–14.

71. Markus SM, Plevock KM, Germain BJS, Punch JJ, Meaden CW, Lee W. Quantitative Analysis of Pac1/LIS1-mediated Dynein Targeting: Implications for Regulation of Dynein Activity in Budding Yeast. Cytoskeleton (Hoboken, NJ). 2011;68(3):157–74.

72. Joglekar AP, Hunt AJ. A simple, mechanistic model for directional instability during mitotic chromosome movements. Biophys J. 2002;83(1):42–58.

73. Sau S, Sutradhar S, Paul R, Sinha P. Budding yeast kinetochore proteins, Chl4 and Ctf19, are required to maintain SPB-centromere proximity during G1 and late anaphase. PLoS One. 2014;9(7):e101294.

74. Rodal A, L LK, Goode B, DG DD, Hartwig J. Actin and septin ultrastructures at the budding yeast cell cortex. Mol Biol Cell. 2005;16:372–384.

75. Winters L, Ban I, Prelogovic M, Kalinina I, Pavin N, Tolic IM. Pivoting of microtubules driven by minus-end-directed motors leads to spindle assembly. BMC Biology. 2019; p. 10.1186/s12915–019–0656–2.

76. Baumgärtner S, Tolić IM. Astral Microtubule Pivoting Promotes Their Search for Cortical Anchor Sites during Mitosis in Budding Yeast. PLoS ONE. 2014;9(4):e93781.

77. Farhadifar R, Baer CF, Valfort AC, Andersen EC, Muller-Reichert T, Delattre M, et al. Scaling, selection, and evolutionary dynamics of the mitotic spindle. Curr Biol. 2015;25(6):732–740. doi:10.1016/j.cub.2014.12.060.

78. Kwon M, Godinho SA, Chandhok NS, Ganem NJ, Azioune A, Thery M, et al. Mechanisms to suppress multipolar divisions in cancer cells with extra centrosomes. Genes & Development. 2008;22:2189–2203.

79. Gergely F, Basto R. Multiple centrosomes: together they stand, divided they fall. Genes & Development. 2008;22:2291–2296.

80. Marthiens V, Piel M, Basto R. Never tear us apart - the importance of centrosome clustering. Journal of Cell Science. 2012;125:3281–3292.

81. Balasubramanian MK, Bi E, Glotzer M. Comparative Analysis of Cytokinesis in Budding Yeast, Fission Yeast and Animal Cells. Current Biology. 2004;14:R806–R818.

82. Holy TE, Leibler S. Dynamic instability of microtubules as an efficient way to search in space. PNAS. 1994;91 (12):5682–5685.

83. Mitchison T, Kirschner M. Dynamic instability of microtubule growth. Nature. 1984;312:237–242.

84. Kirschner M, Mitchison T. Beyond self-assembly: From microtubules to morphogenesis. Cell. 1986;45:329–342.

85. Laan L, Pavin N, J JH, Romet-Lemonne G, van Duijn M, Lopez MP, et al. Cortical dynein controls microtubule dynamics to generate pulling forces that position microtubule asters. Cell. 2012;148(3):502–14.

86. Pavin N, Laan L, Ma R, Dogterom M, Jülicher F. Positioning of microtubule organizing centers by cortical pushing and pulling forces. New Journal of Physics. 2012;14:105025.

87. Ma R, Laan L, Dogterom M, Pavin N, Jülicher F. General theory for the mechanics of confined microtubule asters. New Journal of Physics. 2014;16:013018.

88. Grill SW, Kruse K, Jülicher F. Theory of Mitotic Spindle Oscillations. Phys Rev Lett. 2005;94:108104.

89. Gittes F, Meyhöfer E, Baek S, Howard J. Directional loading of the kinesin motor molecule as it buckles a microtubule. Biophys J. 1996;70:418–429.

Mechanisms of MTOC clustering and spindle positioning in the budding yeast *Cryptococcus neoformans*: a microtubule grow-and-catch model - S1 Text

Saptarshi Chatterjee[1], Subhendu Som[1], Neha Varshney[2¤], Kaustuv Sanyal[2*], Raja Paul[1**]

1 School of Mathematical and Computational Sciences, Indian Association for the Cultivation of Science, Kolkata -700032, India

2 Molecular Mycology Laboratory, Molecular Biology and Genetics Unit, Jawaharlal Nehru Centre for Advanced Scientific Research, Jakkur, Bangalore -560064, India

¤Current Address: Ludwig Institute for Cancer Research, Department of Cellular and Molecular Medicine, University of California San Diego, La Jolla, CA 92093, USA

* sanyal@jncasr.ac.in ** raja.paul@iacs.res.in

One-dimensional mathematical model describing the forces due to localized dynein organization in the daughter bud cell cortex:

In the mathematical template, we assume that the dynein density in the mother cortex is uniform as considered in the earlier scenario. However, in the daughter cortex the dyneins are spatially localized as discrete patches of length l_1 with the gap between two consecutive patches being l_2. We further assume that the effective dynein density within a patch falls exponentially with distance. Hence,

$$\lambda^D_{dyn}(s) = \lambda^D_{dyn}(0)e^{-s/\xi^D_{dyn}} \tag{1}$$

Here, $\lambda^D_{dyn}(0)$ denotes the effective dynein density at the intersection of the axis of symmetry and the daughter cortex. ξ^D_{dyn} is an external tunable parameter in the current model which dictates how the effective dynein density drops off within the patch as one moves away from the intersection of the axis of symmetry and the daughter cortex in the transverse direction along the daughter cortex. It is evident from the present model construction that the net contribution to $F^{cor(D)}_{dyn(sliding)}$ will come from the discrete patches only. Hence the integration

$\int_0^{l^D_{arc}}$ will have nonzero finite contributions from $\int_0^{l_1} + \int_{l_1+l_2}^{l_2+2l_1} + ...$ only. Now the expression for $F^{cor(D)}_{dyn(sliding)}$ reads,

$$\begin{aligned}
F^{cor(D)}_{dyn(sliding)} &= B_D \int_0^{l^D_{arc}} ds\ e^{-(d+r_D-x-a+s)/L^{av}_{MT}} \lambda^D_{dyn}(s) \\
&= B_D \lambda^D_{dyn}(0) \int_0^{l^D_{arc}} ds\ e^{-(d+r_D-x-a+(1+\gamma)s)/L^{av}_{MT}} \\
&= B_D \lambda^D_{dyn}(0) \Bigg[\int_0^{l_1} ds\ e^{-(d+r_D-x-a+(1+\gamma)s)/L^{av}_{MT}} + \\
&\quad \int_{l_1+l_2}^{l_2+2l_1} ds\ e^{-(d+r_D-x-a+(1+\gamma)s)/L^{av}_{MT}} + \int_{2l_2+2l_1}^{2l_2+3l_1} ds\ e^{-(d+r_D-x-a+(1+\gamma)s)/L^{av}_{MT}} + ... \Bigg] \\
&= \frac{B_D \lambda^D_{dyn}(0) L^{av}_{MT}}{(1+\gamma)} e^{-(d+r_D-x-a)/L^{av}_{MT}} \Bigg[1 - e^{-(1+\gamma)l_1/L^{av}_{MT}} + e^{-(1+\gamma)(l_1+l_2)/L^{av}_{MT}} \\
&\quad - e^{-(1+\gamma)(l_2+2l_1)/L^{av}_{MT}} + e^{-(1+\gamma)(2l_2+2l_1)/L^{av}_{MT}} - e^{-(1+\gamma)(2l_2+3l_1)/L^{av}_{MT}} + ... \Bigg] \qquad (2)
\end{aligned}$$

In the above expressions we take, $L^{av}_{MT}/\xi^D_{dyn} = \gamma \implies 1/\xi^D_{dyn} = \gamma/L^{av}_{MT}$. Let us reconstruct the above expression for $F^{cor(D)}_{dyn(sliding)}$ by taking,

$$e^{-(1+\gamma)l_1/L^{av}_{MT}} = \mathcal{P} \qquad (3)$$

$$e^{-(1+\gamma)l_2/L^{av}_{MT}} = \mathcal{Q} \qquad (4)$$

Plugging $\mathcal{P}$ and $\mathcal{Q}$ into the expression of $F^{cor(D)}_{dyn(sliding)}$ we obtain,

$$\begin{aligned}
F^{cor(D)}_{dyn(sliding)} &= \frac{B_D \lambda^D_{dyn}(0) L^{av}_{MT}}{1+\gamma} e^{-(d+r_D-x-a)/L^{av}_{MT}} \\
&\quad \Bigg[1 - \mathcal{P} + \mathcal{P}\mathcal{Q} - \mathcal{P}^2\mathcal{Q} + \mathcal{P}^2\mathcal{Q}^2 - \mathcal{P}^3\mathcal{Q}^2 + ... \Bigg] \\
&= \frac{B_D \lambda^D_{dyn}(0) L^{av}_{MT}}{1+\gamma} e^{-(d+r_D-x-a)/L^{av}_{MT}} \Bigg[1 - \mathcal{P}(1-\mathcal{Q}) \frac{1-(\mathcal{P}\mathcal{Q})^n}{1-\mathcal{P}\mathcal{Q}} \Bigg] \qquad (5)
\end{aligned}$$

where $nl_1 + nl_2 \simeq nl_1 + (n-1)l_2 \simeq l^D_{arc}$. Furthermore, only retaining terms up to first order we obtain,

$$F^{cor(D)}_{dyn(sliding)} = \frac{B_D \lambda^D_{dyn}(0) L^{av}_{MT}}{1+\gamma} e^{-(d+r_D-x-a)/L^{av}_{MT}} \Bigg[1 - e^{-(1+\gamma)l_1/L^{av}_{MT}} \Bigg] \qquad (6)$$

It is evident from the above equation that putting $\gamma = 0$ and $l_1 = l^D_{arc}$, we get back the earlier expression with uniform dynein density.

Steric Forces

We have considered steric hindrance between the cell membrane and the spindle. The steric clash between the cell membrane and the spindle is devised via the hardcore repulsion between cell membrane in the mother bud and $SPB(L)$, and between the cell membrane in the daughter bud and $SPB(R)$. The steric repulsion in the mother bud $F^{steric(M)}_{cell-mem}$ is taken as

$$F^{steric(M)}_{cell-mem} = C_M e^{-\zeta_M (R_M + x - a)/L^{av}_{MT}} \tag{7}$$

Similarly, the steric repulsion in the daughter bud $F^{steric(D)}_{cell-mem}$ is

$$F^{steric(D)}_{cell-mem} = -C_D e^{-\zeta_D (d + r_D - x - a)/L^{av}_{MT}} \tag{8}$$

We take $C_M = C_D$ and $\zeta_M = \zeta_D$ since the repulsive forces stemmed at both the mother and daughter cell-membrane upon steric interaction are identical in nature. From the expression, it is also clear that the magnitude of the force solely depends upon the instantaneous overlap between the objects under consideration. Here C_M and C_D refer to the amplitudes of the forces generated due to the steric clashes between cell membrane (mother or daughter) and $SPB(L$ or $R)$. The length scale, more precisely, the short-range limit of the steric forces is governed by ζ_M and ζ_D. As ζ_M (or ζ_D) with nonzero positive value is levelled up, $F^{steric(M \text{ or } D)}_{cell-mem}$ drops sharply with increasing distance.

To include the effect of the finite size of the $SPB(L$ or $R)$ (r_{SPB}), in the steric force expressions R_M is replaced by $R_M \to R_M - r_{SPB}$ and r_D is replaced by $r_D \to r_D - r_{SPB}$ where r_{SPB} is the radius of the SPB.

Analytical model assumptions and comparisons with the agent-based model

The mathematical model construction is based upon several simplifications described in the following: 1. The model does not account for the process of bi-orientation on the NE. We assume a bi-oriented configuration of two SPBs throughout (Fig 3B-3C). In the agent-based model, after SPB duplication, the process of SPB biorientation has been accounted for. 2. In the analytical model, the spindle length is fixed and taken to be $2a$ across the whole range of spatial variation along the axis of symmetry. In the agent-based simulations, spindle length is determined by the forces acting on nMTs as well as cMTs. It is not predetermined.

3. In the one-dimensional analytical model, the motion of the nucleus/ spindle is strictly confined along the X-axis. We only emphasize the translational motion of the spindle of length $2a$ governed by a set of MT mediated forces. The rotational degrees of freedom responsible for the spindle orientation is not considered in the model for simplicity. The spindle is always laid upon the X-axis with its orientation being parallel to the symmetry axis (X-axis). Restricting the spindle movement along the axis of symmetry by default accounts for the net cancellation of forces along the transverse direction since MT nucleation is considered isotropic in all directions. In the agent-based model, simulated on a 3-d geometry, no such restrictions have been imposed (Fig 3A-3C). 4. The analytical model does not include stochastic fluctuations originating from the randomness in MT dynamics in the force balance landscape. The closed-form expressions of the governing forces are evaluated in a time-independent quasi-equilibrium configuration. In the agent-based model, a major source of stochastic fluctuations is the MT dynamic instability [1–4] where an MT randomly switches between growth and shrinkage phase, 5. For simplicity, we have not considered a load-dependent variation of average MT length in the analytical model. However, in the agent-based simulation, load-dependent modulation of the following MT dynamic instability parameters, growth velocity (v_g) and catastrophe frequency (f_c) have been taken into account.

The above-mentioned assumptions and the differences between the analytical and the agent-based model do not alter the overall qualitative attributes of the spindle positioning.

Additional numerical analysis of MTOC clustering (agent-based model)

In several models, it has been shown that cellular processes involving MT mediated 'grow-and-catch' mechanisms are often optimized by the regulation of the number of MTs [5, 6]. In a similar 'search and capture' process, as the MT number increases, the capture time gradually decreases to a threshold timescale followed by a saturation [7]; the scenario implies that upon a stepwise increase in the number of MTs per MTOC, the clustering time is expected to decrease. We further investigated the sensitivity to varying cMT numbers in a case by case fashion; a. the MT number per MTOC is kept constant upon clustering of two MTOCs, b. adding the MT number upon a fusion of the MTOCs up to a maximum limit to 4 MTs per MTOC and then, c. removing the maximum limit respectively (S3 Fig A). We

observe that within the currently explored parameter regime, irrespective of the microscopic mechanisms (a fixed number of MT per MTOC or an increasing number of MTs per MTOC) the clustering of the MTOCs can be achieved within the physiological time scale of 25-30 min. The exact mechanism can only be ascertained by future experiments.

It is demonstrated that MTOCs colocalize with KTs [8, 9] (Fig 2A-2C). In our earlier *in silico* analysis [10], we assumed that the KTs are connected to MTOCs from the beginning of the simulation. We further assumed that each KT is connected to a single MTOC. In the model, at the onset of the simulation, the objects that cluster to form an SPB are taken to be MTOC-KT pairs as depicted in the cartoons of Fig 2C, Fig 3A, S2 Fig A-E. In this setting, as the MTOCs cluster, KTs also cluster in unison. Therefore, the MTOC clustering time and KT clustering time remain synonymous when the number of KTs per MTOC is chosen to be unity. Note that the total number of MTOCs is fixed at 14 (as the number of KTs/chromosomes in each cell) at the onset of simulation. Next, we relaxed the assumption of single KT per MTOC and examined what happens to the KT clustering if one or more KTs are attached to the MTOCs at the beginning (S3 Fig B). However, the total number of MTOCs and KTs are kept fixed at the onset of the simulation, as before. Our model predicted that if more than one KT is attached to an MTOC, the KT clustering process is marginally faster than the MTOCs (S3 Fig B). Consider the situation where more than one KT is attached to an MTOC, but the total number of KTs and the total number of MTOCs are equal and fixed at 14. Therefore, few MTOCs would be there which are not attached to any KT. Complete KT clustering requires the clustering of only those MTOCs which are associated with KTs. However, complete MTOC clustering involves the fusion of both the following set of MTOCs: (a) MTOCs attached to KTs, (b) MTOCs not associated with any KT. In that scenario, we expect that time taken for all the KTs to cluster would be less than that of MTOC clustering. Therefore, in the outcomes of the present model construction, the marginal time difference in the clustering times of KTs and MTOCs arises which is evident from S3 Fig B.

Next, we estimated the time it would take when both the following mechanisms: (a) inter cMT coupling at NE and (b) MT-cell cortex interaction with suppressed dynein and enhanced Bim1 bias are acting concomitantly. Note that, in the currently explored model parameter regime, both the mechanisms are capable of rendering complete MTOC clustering within the physiological time limit of about 25-30 min (Fig 2, 4B-4E, Table 2) [10]. Now, if

the mechanism of MT-cell cortex interaction (with suppressed dynein and enhanced Bim1 bias) is turned on alongside the mechanism of inter cMT coupling at NE, we expect that the clustering time would further reduce. In the model analysis, we tuned the level of Bim1 bias when both the mechanisms are at play. As expected, increased Bim1 bias alongside inter cMT coupling further reduces the clustering time up to a certain time limit, in the currently explored parameter regime (S3 Fig C).

Additional numerical analysis of spindle positioning (analytical model)

Instantaneous push from the mother and the daughter cortex forces the spindle to localize in mother bud

From the analytical model geometry (Fig 3B-3C) and S7 Fig A, it is clear that the instantaneous push from the mother and the daughter cortex are oppositely directed. In the expressions for the instantaneous pushing forces $F_{push-inst}^{cell-mem(M)}$ and $F_{push-inst}^{cell-mem(D)}$, the percentage of MTs experiencing instantaneous cortical push is determined by A_M and A_D respectively. We varied this percentage as a tunable parameter of the system with the pre-imposed constraint $A_M = A_D$ for this particular case. Since the daughter bud size is smaller than the mother bud, the balancing act between these two competing forces leads to a stable spindle position inside the mother bud (S7 Fig A). A configuration with equal mother and daughter bud size would lead to a stable spindle position at the center of the septin ring. Importantly, due to the very nature of the force which pushes the $SPB(L$ and/or $R)$ away from the cell membrane mother and/or daughter, in the resultant force balance landscape, only stable fixed points of the spindle position appear (S7 Fig A).

In the sole presence of cortical pull from mother and daughter, spindle collapses onto the cortex

The sole presence of cortical pull from the mother and daughter cortex gives rise to unstable fixed points of the spindle position in the force balance contour for various spindle positions. In a parameter space mapped by λ_{dyn}^{M}= 4.0 μm $^{-1}$, λ_{dyn}^{D} = 5.0 μm^{-1}, we varied $B_M(= B_D)$ and observed that stable fixed points of the spindle position in the mother and daughter cortex with a slew of unstable fixed points sandwiched in between (S7 Fig B). The

unstable fixed points of the spindle close to the septin ring indicate that either the spindle collapses onto the mother cortex or the daughter cortex while slightly displaced from the unstable fixed point of the spindle position depending upon the direction of perturbation.

Tug of war between cortical push and pull leads to a collapse of the spindle onto the cortex

We first considered a theoretical mechanistic framework, where force transduction only either from the mother cortex or the daughter cortex is allowed. In that construction, we observe a sharp spatial transition of the spindle from the daughter (mother) cortex to mother (daughter) cortex upon step-wise increase in dynein density in mother (daughter) cortex as depicted in S7 Fig C (relevant parameters: $A_M = 5$ pN, $A_D = 5$ pN, $B_M = 5$ pN, $B_D = 5$ pN, wherever applicable). Next, we carried out a sensitivity analysis in a scenario where the instantaneous cortical push and dynein mediated cortical pull stemming from both the mother and daughter cortex are present (Fig 6A, S7 Fig D). We varied the dynein density in the mother cortex λ^M_{dyn} keeping the dynein density in the daughter cortex λ^D_{dyn} fixed at 8.0 μm^{-1} and vice versa (D_M=D_D=0; other parameters fixed at base values as shown in Table 1; λ^M_{dyn} fixed at 5.0 μm^{-1}, when λ^D_{dyn} is varied). The force balance showcases that for lower values of dynein density in the mother cortex, cortical pull from the daughter (λ^D_{dyn} fixed at 8.0 μm^{-1}) paired with the instantaneous push from the mother bud dominate leading to a spatial collapse of the spindle onto the daughter cortex marked by the stable fixed points of the spindle position in the daughter cortex. As the dynein density in the mother cortex (λ^M_{dyn}) is gradually increased, cortical pull from the mother cortex takes the driver's seat. Subsequently, the dominant cortical pull from the mother cortex initiates a spatial transition of the spindle to the mother cortex via a string of unstable fixed points of the spindle position marked by the oblique segment of the 'Z' contour (S7 Fig D). Similarly, when dynein density in the mother cortex (λ^M_{dyn}) is kept fixed at 5 μm^{-1} and dynein density in the daughter cortex (λ^D_{dyn}) is varied, we observe a spatial collapse of the spindle onto the daughter cortex at higher values of λ^D_{dyn} with an intermediate regime having three fixed points of the spindle position (stable fixed points at the mother and the daughter cortex with unstable fixed points wedged in between) as discernible in the inverted 'Z' contour (Fig 6A). We also obtain fixed point contour of the spindle position having stable fixed points at the mother and daughter cortex with unstable fixed points located in between when average

MT length (L_{MT}^{av}) is varied (S7 Fig E) keeping other relevant parameters fixed (Table 1 and $\lambda_{dyn}^{M} = 5\ \mu\text{m}^{-1}$, $\lambda_{dyn}^{D} = 10\ \mu\text{m}^{-1}$).

Combination of MT buckling with cortical push and pull prevents collapse, maintains stable spindle position near septin ring

Allowing force transduction solely either from the mother cortex or the daughter cortex in presence of MT buckling, the stable fixed points of the spindle position make a spatial transition toward the mother (daughter) cortex from the daughter (mother) cortex upon a gradual increase in cortical dynein density λ_{dyn}^{M} or λ_{dyn}^{D} (S7 Fig F). It is imperative to note that unlike previous scenarios, in presence of MT buckling, the spindle does not collapse onto the cortical region, rather localizes $\simeq 0.5\ \mu$m away from the cortex (S7 Fig F) in the currently explored parameter regime. It is evident from the expression of the buckling forces $F_{buckle}^{cor(M)}$ and $F_{buckle}^{cor(D)}$ that in the vicinity of the cortex the force generated due to MT buckling shoots up to a very high value. Since the force due to MT buckling is of 'pushing' nature, it pushes the spindle away from the cortex, thus preventing the spindle from collapsing onto the cortex. In presence of MT buckling transition in both the mother and daughter cortex, the balancing act between the governing forces ($F_{push-inst}^{cell-mem(M\ \text{and}\ D)}$, $F_{dyn}^{cor(M\ \text{and}\ D)}$, $F_{buckle}^{cor(M\ \text{and}\ D)}$), leads to a stable positioning of the spindle within the daughter bud in the vicinity of the septin ring (Fig 6B-6C). We observed that upon step-wise increment in the dynein density within the daughter cortex (λ_{dyn}^{D}), the stable fixed point contour of the spindle position tend to shift deep inside the daughter cortex owing to an enhancement in the net force directed toward the daughter cortex as shown in Fig 6B (relevant parameters: $\lambda_{dyn}^{M} = 3.0\ \mu\text{m}^{-1}$, other parameters as in Table 1). We also carried out sensitivity analysis on the robustness of the stable spindle positioning close to the septin ring within the daughter bud upon variation in the average MT length (L_{MT}^{av}). We find that across a reasonably significant range of L_{MT}^{av} values, the location of the stable fixed point for the spindle remains unperturbed within the daughter bud (Fig 6C, relevant parameters: $\lambda_{dyn}^{M} = 3.0\ \mu\text{m}^{-1}$, $\lambda_{dyn}^{D} = 10.0\ \mu\text{m}^{-1}$, other parameters as in Table 1).

Differential spatial arrangement of dyneins in mother and daughter cortex results in force balance landscape with stable as well as unstable positions of the spindle

Our previous study [10] indicates that the spatial arrangement of dyneins in the mother and daughter cortex is different. The dynein puncta in the mother cortex are uniformly distributed, whereas in the daughter cortex a large localized dynein punctum near the axis of symmetry is observed. This differential spatial arrangement alludes to the fact that for proper nuclear migration (e.g. proper spindle positioning) a directed pull from the daughter cortex on the nucleus is crucial to navigating the nucleus inside the daughter bud. Further, we also observed that irrespective of whether the cortical milieu is enriched with uniform dynein distribution at both the mother and the daughter cortex or the differential distribution as mentioned above, the innate mechanistic perspective relies upon the net pulling force generation from the daughter cortex. This leads to a question that how the force balance landscape governing the spindle positioning behaves when one makes a gradual transition from localized puncta in the daughter cortex to a full-fledged uniform distribution. To address that we assign a characteristic length scale ξ_{dyn}^{D} with the effective localized dynein puncta within the daughter cortex. As ξ_{dyn}^{D} is increased, the effective spatial profile of dyneins within the daughter cortex makes a gradual changeover to a uniform distribution. With this mathematical template at hand, we carried out sensitivity analysis on the force balance landscape governed by various MT mediated forces (e.g. instantaneous push, dynein pull, MT buckling transition) upon the variation in the parameter ξ_{dyn}^{D}. In presence of instantaneous push and dynein pull from the daughter (with no force transduction from the mother cortex and no MT buckling), the gradual increment in ξ_{dyn}^{D} leads to an enhancement in the dynein pull from the daughter invoking a spatial changeover of the spindle from the mother cortex to the daughter cortex (S7 Fig G). For lower values of ξ_{dyn}^{D}, instantaneous push dominates the force balance landscape shoving the spindle onto the mother cortex (marked by the stable fixed-point contour of the spindle position in the mother cortex). Furthermore, in sole presence of dynein pull from both the mother and the daughter cortex, the variation in ξ_{dyn}^{D} yields null force contours (the inverted 'Z' contour) having stable fixed points of the spindle position at the mother and the daughter cortex and a string of unstable fixed points of the spindle location sandwiched in between (S7 Fig H). The gradual increase in ξ_{dyn}^{D} leads to stable fixed points of the spindle position inside the daughter cortex, around

~ 0.5 μm away from the septin ring when instantaneous push, dynein pull and MT buckling at both the mother and daughter cortex act alongside each other (S7 Fig I) in the currently explored parameter regime. Stable spindle positioning at higher values of ξ^D_{dyn} (referring to the uniformity within the spatial organization of dyneins) further corroborates with the 'agent-based' simulation which includes uniform distribution of dyneins in both mother and daughter cortex as depicted in S5 Fig A, S5 Fig B, S5 Fig D and Fig 6E (third bar), Fig 6F. The spindle localization is observed to be at a distance ~ 1 μm from the septin ring inside the daughter bud (S5 Fig A, S5 Fig B, S5 Fig D, Fig 6E, third bar, and Fig 6F).

References

[1] T. E. Holy and S. Leibler, PNAS **91 (12)**, 5682 (1994).

[2] M. Dogterom and S. Leibler, Physical Review Letters **70(9)**, 1347 (1993).

[3] T. Mitchison and M. Kirschner, Nature **312**, 237 (1984).

[4] M. Kirschner and T. Mitchison, Cell **45**, 329 (1986).

[5] Z. Bertalan, Z. Budrikis, C. A. M. L. Porta, and S. Zapperi, PLOS ONE p. 10.1371/journal.pone.0141305 (2015).

[6] R. Wollman, E. Cytrynbaum, J. Jones, T. Meyer, J. Scholey, and A. Mogilner, Current Biology **15**, 828–832 (2005).

[7] A. Sarkar, H. Rieger, and R. Paul, Biophysical Journal **116**, 2079–2091 (2019).

[8] V. Yadav and K. Sanyal, mSphere **3(4)**, e00190 (2018).

[9] L. Kozubowski, V. Yadav, G. Chatterjee, S. Sridhar, M. Yamaguchi, S. Kawamoto, I. Bose, J. Heitman, and K. Sanyal, mBio **4(5)**, 00614 (2013).

[10] N. Varshney, S. Som, S. Chatterjee, S. Sridhar, D. Bhattacharyya, R. Paul, and K. Sanyal, PLoS Genet **15(2)**, e1007959 (2019).